Applied Thermal Engineering 303 (2026) 132227

Contents lists available at ScienceDirect

Applied Thermal Engineering

journal homepage: www.elsevier.com/locate/apthermeng

Research Paper

Flow boiling critical heat flux in MICRO-scale heat sinks and comparison with correlations

Joseph J. Widgington [a], Ali H. Al-Zaidi [b], Tassos G. Karayiannis [a,*]

[a] Centre for Energy Efficient and Sustainable Technologies, Brunel University of London, Uxbridge UB8 3PH, UK
[b] University of Misan, Al-Amarah, 62001, Iraq

ARTICLE INFO

Keywords:
Micro-scale
Single Channel
Multi-channels
Flow boiling
Critical heat flux
Correlations

ABSTRACT

The growing demand for high-performance miniature electronics is forcing the heat dissipation requirements to increasingly higher levels. Flow boiling in micro-scale heat exchangers is a good choice for cooling these high heat flux devices. In such systems, the prediction of critical heat flux (CHF) is a crucial aspect in thermal-fluid system design, as it defines the maximum limits of thermal management systems. Different CHF mechanisms were identified and studied in the literature, leading to the development of numerous correlations. However, significant discrepancies still exist among these studies. The present study investigated experimentally the critical heat flux of HFE-7100 in single and multi-channels heat sinks. Saturated flow boiling experiments were conducted at inlet pressure of 1, 1.5 and 2 bar, inlet subcooling of 5 K and 10 K and mass flux of 100–750 kg/m^2 s. The wall heat flux was increased gradually until the CHF was reached at 435 kW/m^2 and 308.6 kW/m^2 for the single channel and the multi-channels, respectively. Events leading to the CHF occurrence were identified in the present study using a high-speed, high-resolution camera and thermocouple readings. The present results were also used to evaluate eight flow boiling CHF correlations, with some found to agree with the current experimental data. In the present study, both mass flux and inlet pressure had a noticeable effect on the CHF phenomenon. However, the effect of inlet pressure remains to be properly evaluated and included in these correlations.

1. Introduction

Ongoing efforts towards the global electrification of a broad-spectrum of industries are presenting new emerging thermal challenges. Insulated gate bipolar transistor (IGBT) modules, commonly utilised in electric trains, high-voltage DC power systems, robotics, motor drives, and smart grids, are approaching heat flux levels of up to 500 kW/m^2 [1,2]. Processors in the information technology sector are generating heat fluxes nearing 460 kW/m^2, with the heat flux of advanced server equipment chips reaching up to 1 MW/m^2 [3,4]. Forced air-cooling methodologies, such as the fans used in typical personal home desktop computers are typically capable of dissipating heat fluxes up to 10 kW/m^2. The absolute upper limit of enhanced forced liquid cooling is effective for heat fluxes below 800 kW/m^2 [5]. Therefore, although forced liquid cooling can be applied for low and moderate heat flux applications, several thermal issues are associated with this technique, such as low overall heat transfer coefficient and non-uniform surface temperature distribution and required high mass flow rates. Consequently, current technology cooling requirements are approaching and exceeding the upper limits of single-phase cooling capabilities. The flow boiling in microchannels has the capability to remove extremely high heat loads per unit area, with multiple studies reporting heat fluxes reaching well over 1 MW/m^2 [6–8]. In addition, this can be achieved while maintaining a fairly uniform temperature of the substrate or electronic device to be cooled. This is a result of large heat transfer surface area to flow area ratios and the utilisation of latent heat [9]. In these designs, it is important to clarify the operational limits. The upper limit is the critical heat flux, which represents the threshold beyond which a further increase in heat flux leads to a significant decline in heat transfer rates [10]. Exceeding the CHF can cause a rapid escalation in surface temperature, potentially leading to thermal failure.

Fundamentally, CHF is reached in both pool and flow boiling due to a considerable reduction in the local heat transfer rates that occur as a result of insufficient contact between liquid and the wall resulting in the formation of an insulating vapour layer [11]. In pool boiling systems, heat is, at first, transferred through convection currents in the natural convection regime, with no bubble formation. The onset of nucleate

* Corresponding author at: Brunel University of London, Uxbridge, Middlesex, UB8 3PH, UK.
E-mail address: tassos.karayiannis@brunel.ac.uk (T.G. Karayiannis).

https://doi.org/10.1016/j.applthermaleng.2026.132227
Received 9 February 2026; Received in revised form 26 April 2026; Accepted 2 July 2026
Available online 4 July 2026

Nomenclature

A	Area, [m^2]
C	Constant, [−]
cp	Specific heat capacity, [J/kg K]
D_h	Hydraulic diameter, [m]
D_{th}	Threshold diameter, [m]
f	Friction factor, [−]
F_i	Inertia force, [N]
F_p	Evaporation momentum force, [N]
F_σ	Surface tension force, [N]
g	Gravitational acceleration, [m/s^2]
G	Mass flux, [kg/m^2 s]
h	Heat transfer coefficient, [W/m^2 K]
$\bar{h}$	Average heat transfer coefficient, [W/m^2 K]
H	Height, [m]
i	Specific enthalpy, [J/kg]
i_{lg}	Latent heat of vaporisation, [J/kg]
k	Thermal conductivity, [W/m K]
L	Length, [m]
La	Laplace number, [−], $La = \rho\sigma D_h/\mu^2$
m	Fin parameter, [−]
$\dot{m}$	Mass flow rate, [kg/s]
MAE	Mean absolute error, [%]
n	Number of data points, [−]
N_{ch}	Number of channels, [−]
$\overline{Nu}$	Average Nusselt number, [−]
P	Pressure, [Pa]
Q	Heat rate, [W]
q''	Heat flux, [W/m^2]
Ra	Average surface roughness, [µm]
r	Vapour core radius, [m]
Re	Reynolds number, [−], $Re = GD_h/\mu$
Sa	Average surface roughness of scanned area, [µm]
t	Time, [s]
T	Temperature, [K]
T_∞	Ambient Temperature, [K]
u	Velocity. [m/s]
U	Absolute uncertainty, [−]
W	Width, [m]
We	Weber number, [−], $We = G^2D_h/\sigma\rho$
x	Vapour quality, [−]
X	Measured parameter, [−]
y	Vertical distance between thermocouples, [m]
z	Distance measured from inlet to end of heated length, [m]

Greek symbols

α	Void fraction, [−]
δ	Film thickness, [m]
ΔP	Pressure drop, [Pa]
ΔT	Temperature difference, [K]
η	Fin efficiency, [−]
θ	Dynamic receding contact angle, [°]
μ	Viscosity, [Pa s]
ρ	Density, [kg/m^3]
$\bar{\rho}$	Average density, [kg/m^3]
σ	Surface tension, [N/m]
τ	Shear stress, [Pa]
Υ	Thermal conductance, [W/K]

Subscript

b	Base
ch	Channel
col	Columns
cr	Critical
cu	Copper
exp	Experimental value
f	Fluid
g	(Vapour)
$heat$	Heated
i	interface
in	Inlet
l	Liquid
$meas$	Measured
out	Outlet
pl	Plenum
$pred$	Predicted value
sat	Saturation
sc	Sudden contraction
se	Sudden expansion
sec	Cross-section
sp	Single-phase
sub	Subcooled
top	Top cover plate
th	Thermocouple
tp	Two-phase
ts	Top surface
w	Wall
z	Axial location

boiling then occurs at greater wall superheats, where bubbles begin to form at nucleation sites on the heated surface [12]. Greater bubble formation and departure occur as the wall superheat intensifies, enhancing heat transfer due to latent heat absorption and increased fluid mixing. Eventually, the number of nucleation sites on the surface and the bubble departure rate is so great that the bubbles coalesce and form bubble columns or jets [13]. Finally, the process reaches the CHF. Beyond the CHF a vapour blanket forms on the heated surface, significantly reducing heat transfer rates and transitioning the system towards film boiling [14]. This vapour blanket causes the wall temperature to rise drastically, which may cause considerable damage to the substrate that is being cooled and devastating system failure. In flow boiling, CHF is also inherently linked to the phenomenon known as dryout, which details a scenario in which parts of the channel wall are no longer in contact with the liquid phase [15]. Whilst CHF fundamentally occurs due to this lack of contact between the wall and the liquid phase, various theories have been proposed regarding the mechanisms through which the onset of dry-out occurs. The next sections present a discussion on different CHF mechanisms and flow boiling CHF correlations.

1.1. CHF Mechanisms

1.1.1. Subcooled Boiling

The reported CHF mechanisms can be separated into two distinct categories, namely subcooled CHF mechanisms and saturated CHF mechanisms [16]. Kim and Mudawar [17] outlined a subcooled CHF mechanism in microchannels referred to as departure from nucleate boiling (DNB), a phenomenon also documented by [18–21] for microchannels, conventional sized channels and flows in microgravity. CHF occurs when a vapour film forms along the heated walls of the channel, even though liquid continues to flow through the central region, as illustrated in Fig. 1. This leads to a rapid and significant increase in wall temperature, indicating a drastic decline in heat transfer performance. This typically occurs under conditions of high mass flux and intense heat

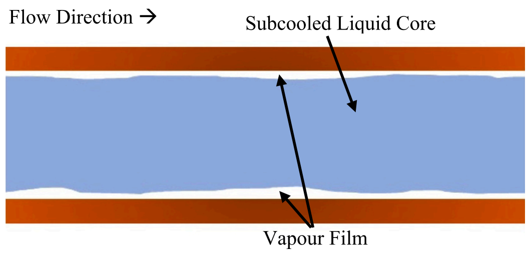

Fig. 1. Departure from nucleate boiling CHF mechanism.

input in strongly subcooled flows.

Another subcooled CHF mechanism that has been frequently reported in literature [22–24] involves the phenomenon of bubble congestion or bubble overcrowding in both macro and micro scales. This occurs when the boundary layer near the heated channel wall becomes densely packed with vapour bubbles. The number of bubbles that form on the heated surface increases such that the surface becomes so crowded that newly formed bubbles are unable to detach, leading to the formation of dry spots on the heater. Bubbles produced at the overheated surface often condense upon entering the cooler main flow, and the interplay between rapid bubble growth and collapse causes significant disturbances in the boundary layer [25]. Additionally, the excessive rate of bubble production hinders the rewetting of the heated surface, as bubble accumulation physically obstructs liquid contact [26], leading to CHF.

A third subcooled CHF mechanism was proposed by Kirby et al. [27] in conventional sized channels, which centred on the development and stability of a dry macro-layer beneath vapour bubbles. A model was developed based on subcooled boiling of water at 1.72 bar. The model proposes that the thin liquid film beneath the bubbles evaporates more quickly than it can be resupplied when the wall temperature reaches a critical threshold. This results in the emergence of dry regions directly under the bubbles, causing a sharp decline in local heat transfer rate and eventually initiating the onset of CHF.

Tong and Hewitt [28] outlined a dryout-based CHF mechanism applicable to both subcooled and saturated boiling regimes in the macro scale, in which an excessively high wall heat flux can fully vaporise the thin liquid film that separates the heated surface from an adjacent vapour slug. This leads to the creation of localised dry spots, resulting in a sharp increase in wall temperature and ultimately triggering CHF. Expanding upon this idea, Liu et al. [29] proposed a mechanistic CHF model in which vapour blankets are formed through the merging of detached bubbles. The extent of these blankets is determined by the departure diameter of individual bubbles, constrained by nearby vapour formations. The blanket stretches downstream and becomes fragmented due to Helmholtz instabilities as the thin liquid layer beneath the vapour blanket evaporates. CHF is considered to occur when this sub-layer is completely exhausted, leaving parts of the heated wall directly exposed to vapour.

Studies using the same fluid as the current work include the work of Lee and Mudawar [30]. They carried out an experimental study using HFE-7100 at subcooled flow boiling conditions. A rectangular multi-channels heat sink made of copper was tested in this study at different channel hydraulic diameters of 0.176–0.416 mm. They performed these experiments at a mass flux of 670.5–2345.5 kg/m^2 s and inlet subcooling of 45.2–97.6 K. Their results showed that the critical heat flux was reached due to the occurrence of vapour blanket on the surface although a liquid core was found in the channels. This is similar to the CHF phenomenon of the departure from nucleate boiling, mentioned above. They also reported that the CHF increased with increasing both mass flux and inlet sub-cooling. In addition, the CHF was found to increase with decreasing channel hydraulic diameter due to the large fluid velocity at a given total mass flow rate. The authors also developed a systematic technique to modify existing correlations for subcooled boiling CHF.

1.1.2. Saturated boiling

In saturated flow boiling, dryout beneath vapour slugs has been proposed as a contributing CHF mechanism. However, the primary focus during saturated boiling remains dryout associated with the annular flow regime. This is because CHF often occurs first within this region, even with low heat fluxes present if the heated length is sufficiently long [31]. This regime is central to numerous investigations into saturated flow boiling, primarily because annular flow is the most commonly observed pattern under such conditions. It is marked by high void fractions and elevated vapour quality, both of which contribute to an increased risk of dryout.

Hewitt [32] identified five distinct dryout mechanisms within the annular flow regime during flow boiling in conventional sized channels, each capable of triggering CHF under specific conditions. These mechanisms, illustrated in Fig. 2, are outlined below:

a) Vapour film: Very high heat fluxes result in a vapour blanket occurring at the channel wall, surrounded by the liquid film. This typically appears at very high heat fluxes with lower vapour qualities.

(b) Deposition and evaporation equilibrium: The CHF condition arises when the evaporation rate of liquid droplets at the heater wall exceeds the deposition rate that occurs at the end of annular flows into the mist flow regime.

(c) Disruption of the liquid film: The liquid film is broken by an unstable surface wave, causing the lower part of the wave to contact the heater wall and dry out.

(d) Dry spot formation: A dry patch forms in the middle of the liquid films, leading to a partial increase in wall temperature. The effect of this dry patch then causes more to form and eventually results in CHF.

(e) Full film dryout: CHF occurs when liquid droplets escape from the film and are carried away by the vapour stream, or when the film completely evaporates.

A unique CHF mechanism specific to microchannel systems is known as early onset dryout. This phenomenon occurs as a result of intense vapour production combined with flow reversal, both of which disrupt the steady delivery of liquid to the heated surface. As vapour generation intensifies, part of the vapour flow can reverse direction, entering the inlet plenum where it mixes with the incoming subcooled liquid. This interaction elevates the liquid temperature towards saturation before it re-enters the microchannels, thereby diminishing its cooling capacity. The reduced thermal margin hastens the development of dryout. This mechanism, depicted in Fig. 3, has been reported by multiple researchers [16,33].

1.2. Existing CHF correlations for flow boiling in microchannels

Appendix A presents eight CHF correlations that are evaluated in the present study. These studies identified different effect of operating conditions and then heat transfer mechanisms. As a result, different control parameters were developed and proposed. In conventional channels, CHF depends strongly on several parameters such as mass flux, inlet subcooling, inlet pressure, channel size (diameter), channel length and working fluids [6]. In micro scale channels, these parameters, along with flow reversal (system instability), surface microstructures and flow maldistribution (in multi-channels), could also affect CHF mechanisms. In the following studies, the effect of mass flux, inlet subcooling, inlet pressure, fluid properties and channel diameter and length are reviewed and discussed.

Bowers and Mudawar [34] proposed a CHF correlation based on flow boiling of R-113 in circular multi-channel heat sinks having inner diameters of 0.51 mm and 2.54 mm with 10 mm length. Their experiments included inlet subcooling ranging from 10 K to 32 K and mass flux of 31–480 kg/m^2 s. They observed that in some cases, the fluid exiting the channels was superheated. A key finding was the lack of an inlet subcooling effect on CHF and the presence of superheated outlet conditions

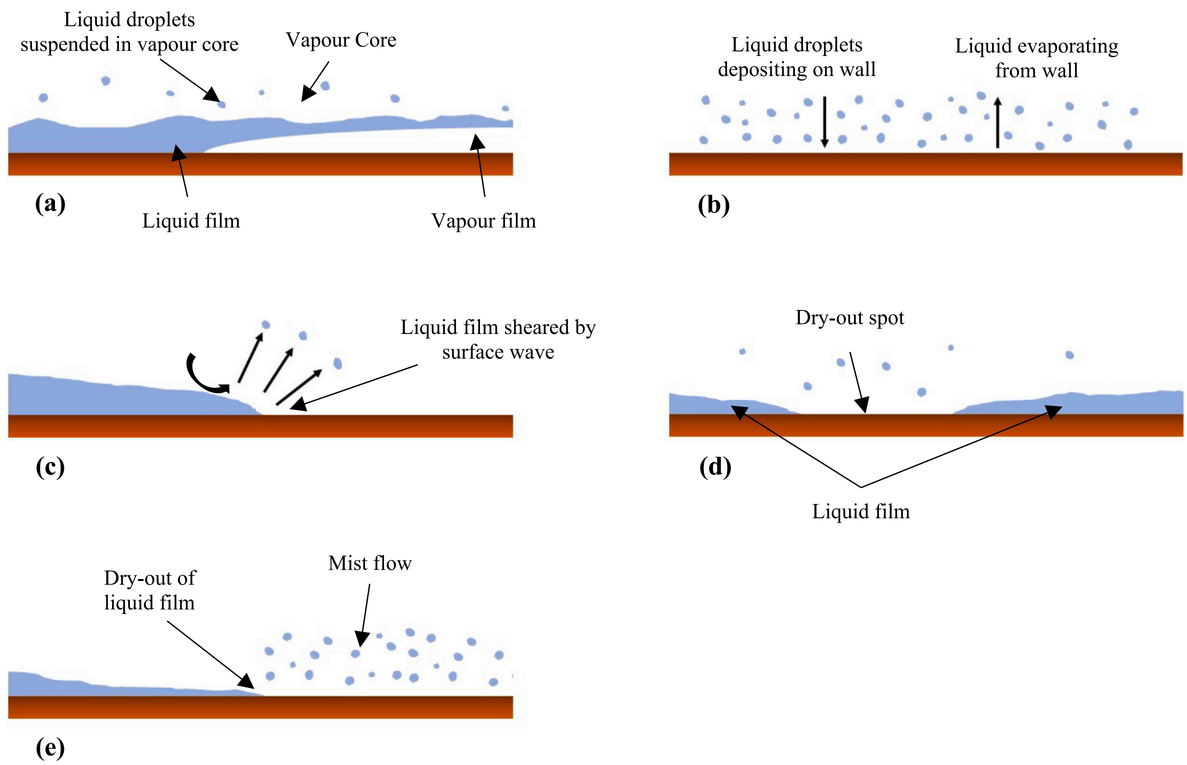

Fig. 2. Mechanisms that cause the onset of boiling during saturated annular flows: (a) vapour film; (b) deposition and evaporation equilibrium; (c) disruption of the liquid film; (d) dry spot formation; (e) full film dryout (modified from [31]).

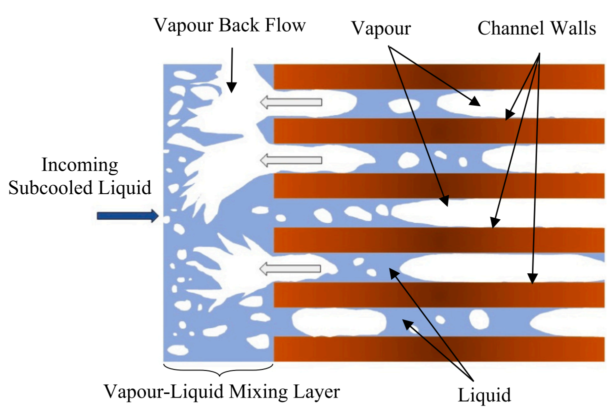

Fig. 3. Vapour backflow into subcooled liquid (modified from [16]).

at the lowest flow rates. Their study found that mass flux had a significant effect on CHF. They then developed a correlation based on an empirical fit of the data.

Qu and Mudawar [16] later measured the CHF for de-ionised water in a micro-channel heat sink containing 21 parallel 0.215 × 0.821 mm channels, each 44.8 mm in length. Mass fluxes between 86 and 368 kg/m^2 s were examined for channel inlet temperatures of 30 °C and 60 °C, i.e. degree of inlet subcooling of 40 K and 70 K. They found that flow instabilities became present as the applied heat flux began to approach the CHF. The flow instabilities then caused flow reversal of the vapour phase into the inlet plenum, thus increasing the temperature at the channel inlet. Consequently, they observed no effect of inlet subcooling between 30 °C and 60 °C as the flow reversal resulted in a loss of subcooling at the inlet. They also reported that the CHF was found to increase with mass flux. A universal microchannel correlation was then proposed based on an empirical fit combining the obtained data for water with the previous study [34] in which R-113 was used. The correlation implies the same relationships as those presented by Bowers and Mudawar [34], with the additional consideration of vapour to liquid density ratio. It proposes that the critical heat flux increases with a decrease in liquid-vapour phase density ratio.

Kuan [35] researched the heat transfer and critical heat flux for flow boiling using R-123 and water in a heat sink containing six 1.054 mm wide × 0.157 mm height microchannels with a length of 63.5 mm. Dryout phenomena were observed to occur in the annular flow regime, where localised dry spots began to appear. A new correlation was empirically developed from their data. They proposed that the critical heat flux was only dependent on the mass flux, latent heat of vaporisation and length-to-diameter ratio, i.e. no other thermophysical properties were relevant.

Kuan and Kandlikar [36] provided a semi-empirical correlation using flow boiling data of water and R-123 in six rectangular multi-channels 63.5 mm in length, having 1.054 mm width and 0.157 mm height. Their model incorporated a force balance framework considering the ratio of evaporation momentum to surface tension forces with the inclusion of inertia forces, illustrated in Fig. 4. As is evident in Fig. 4, this force balance is dependent on the three-phase contact angle. An empirical constant, denoted as C, was calibrated during the correlation

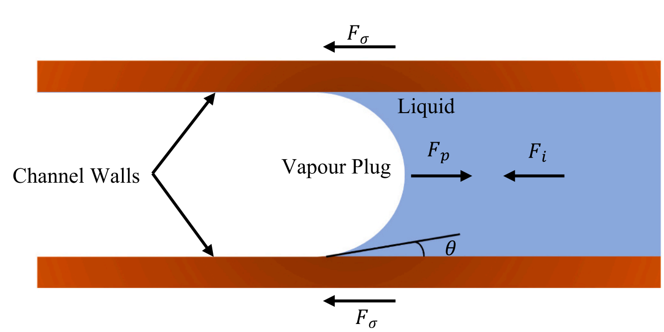

Fig. 4. Liquid-vapour interfacial forces (modified from [36]).

development, with values found to be 0.002679 for both water and R-123, 0.002492 for water alone, and 0.003139 for R-123 alone. It was found that CHF increased with mass flux (Weber number), surface tension, receding contact angle, θ in Fig. 4, and latent heat of vaporisation. In their work, the receding contact angles of water and R-123 on copper surfaces were measured to be 45° and 5°, respectively, using a high-speed photographic technique.

Koşar and Peles [6] developed a CHF correlation based on experiments with R-123 in a microchannel heat sink composed of five parallel channels, each measuring 10 mm in length, 0.2 mm in width, and 0.264 mm in height. They reported that the CHF mechanism was due to the dryout. They also found that the CHF increased with system pressure until a maximum value, after which the CHF then begins to decrease with system pressure. They concluded that an increase in system pressure tends to raise CHF when the liquid-to-vapour density ratio decreases. However, they also noted that other pressure-related effects, specifically the reduction in surface tension and latent heat at higher pressures, can act to decrease the CHF. These competing mechanisms create a non-monotonic relationship, with CHF reaching a peak at an intermediate pressure. In their data, the CHF was also found to increase with increasing mass flux. They proposed a correlation by introducing exit quality, mass flux, latent heat and the ratio of exit pressure to the fluid's critical pressure to capture pressure and property effects.

An empirical CHF correlation was developed by Ong and Thome [37] based on experimental data for R-134a, R-236fa and R-245fa in single, horizontal channels with inner diameters of 1.03 mm, 2.20 mm and 3.04 mm and heated length of 180–540 mm. Additionally, CHF data from experiments by Wojtan et al. [38] for R-134a and R-245fa in microchannel tubes with 0.5 mm and 0.8 mm internal diameter and 20–70 mm long were also incorporated. The data provided by Park [39] for R-134a, R-236fa and R-245fa in microchannels 30 mm in length, with heated diameters of 0.3 mm and 0.8 mm were also used. Certain parametric effects were reported, in addition to the development of a new correlation. Their study found that channel size does not influence the critical heat flux for mass fluxes up to 500 kg/m^2 s. However, beyond this threshold, CHF values began to diverge, with the smallest channel (1.03 mm) exhibiting the highest CHF for both R-134a and R-236fa. The rise in CHF was attributed to confinement effects and the dominance of surface tension and viscosity over inertial and gravitational forces in micro-scale channels. Small channel size leads to high channel confinement number, i.e. high surface tension force. Results also indicated that for R-134a and R-236fa, CHF decreases with rising pressure at a given mass flux, attributed to reduced latent heat at higher pressures. Additionally, comparisons of CHF among R-134a, R-236fa, and R-245fa at a saturation temperature of 31 °C showed that R-245fa exhibited the highest CHF, followed by R-134a, while R-236fa had the lowest. These trends closely correlate with the latent heat values of the fluids, with R-245fa having the highest latent heat and R-236fa the lowest. They also reported that the inlet subcooling was insignificant on the CHF results, while clear mass flux effect was found for the range studied.

Dryout conditions were achieved by Anwar et al. [40] using a range of refrigerants, namely R-134a, R-1234yf, R-152a, R-22, R-245fa, R-290 and R-600a in vertical upward tubes with internal diameters between 0.64 mm and 1.70 mm and 213–245 mm length. They reported that the required heat flux to reach dryout increased with rising mass flux, as higher heat input is needed to fully evaporate the liquid refrigerant and reach critical vapour quality. Interestingly, they reported that dryout heat flux was largely independent of saturation temperature (system pressure). This was explained as the result of two competing effects: while increasing the saturation temperature reduces the liquid-to-vapour density ratio, thereby stabilising the thin liquid film and promoting higher dryout heat flux, it simultaneously reduces the latent heat of vaporisation, which would otherwise decrease the heat input required to reach dryout region. These counteracting influences were believed to balance out, resulting in negligible net change in dryout heat flux across the tested temperature range. Additionally, they found that larger tube diameters corresponded to higher dryout heat fluxes, likely due to increased mass flow rates and reduced shear stress at the wall, which aided in maintaining the liquid film. The resulting correlation was developed based solely on hydraulic diameter-to-heated length ratio, mass flux and latent heat, under the assumption that thermophysical property effects, such as surface tension or density ratios, were negligible.

Tibiriça et al. [41] developed a correlation from an empirical fit from a data bank that included water, R-113, R-12, R-134a, R-123, R-236fa, R-245fa, R-1234z(e) and Nitrogen in single channels with inner diameters between 0.24 mm and 6.92 mm at mass fluxes between 23.6 and 8800 kg/m^2 s. Their correlation was developed through direct empirical fitting and did not involve a detailed mechanistic or parametric analysis. However, the correlation predicts that critical heat flux increases with mass flux, latent heat of vaporisation and decreases with Laplace number, Weber number and liquid-to-vapour density ratios.

Tibiriça et al. [42] also carried out another experimental study to examine the effect of different parameters on saturated flow boiling CHF of R-134a and R-245fa. These two fluids were tested in a horizontal stainless-steel tube having 2.2 mm diameter and 154 mm to 361 mm heated lengths. Their operating conditions were set at a mass flux of 100–1500 kg/m^2 s and exit saturation temperatures of 25, 31 and 35 °C. They reported that CHF increased with increasing inlet subcooling and mass flux. They noted that higher heat flux is required to achieve the same vapour quality when increasing one of these parameters. They also mentioned that CHF was found to decrease with increasing channel length and saturation temperature (system pressure). The authors explained this length effect as follows: reducing channel length can reduce the heat transfer area and thus higher heat flux should be supplied to achieve the same vapour quality. The authors [41] mentioned that the reduction in the latent heat of vaporisation with increasing saturation temperature was the reason for this reduced CHF. Their results also showed that R245fa had higher CHF than R134a due to the higher latent heat.

The studies reviewed demonstrate that critical heat flux in microchannels and mini-channels is governed by a complex interplay of thermophysical properties, flow parameters, and channel geometry. Mass flux consistently emerges as a dominant factor, with higher values generally leading to increased CHF. Several studies found negligible influence of inlet subcooling on CHF [16,34,37]. In contrast, increasing inlet subcooling leads to higher CHF as reported by [42]. Pressure effect was reported to be more complex: (i) insignificant effect due to the balance between liquid-to-vapour density ratio and latent heat of vaporisation [40], (ii) inverse effect due to the reduction in latent heat of vaporisation [37,42], and (iii) positive and then inverse effects due to the competing mechanisms of density ratio, surface tension and latent heat [6]. Increasing channel size leads to increase CHF [40], while insignificant and then inverse effects were found by [37], based on their mass flux ranges. Shorter channel length results in a higher critical heat flux, see [42]. Other control parameters such as receding contact angle θ and average density $\overline{\rho}$, were also considered, resultant from the force balance proposed by [36] and presented in Fig. 4. Overall, no single parameter, except the mass flux, universally dominates across all conditions, emphasizing the need for multi-parameter correlations that accurately capture this complex interplay between parameters.

The objectives of the present study are to experimentally determine the critical heat flux of HFE-7100 in microchannels using high-speed flow visualisation and precise thermal measurements, and to identify the underlying dryout mechanisms responsible for CHF. Single and multi-channels configurations are examined at different operating conditions. The study aims to improve understanding of key parametric effects, such as the change in fluid properties as a result of pressure, mass flux and heat transfer characteristics, on CHF behaviour. Additionally, the performance of existing CHF correlations is evaluated, with attention given not only to their predictive accuracy but also to the physical relevance of the assumptions on which they are based.

2. Experimental methodology

2.1. Experimental facilities

The experimental facilities used to investigate flow boiling of HFE-7100 in a multi-channel heat sink and in a single microchannel have been discussed extensively in [43,44], respectively. Schematics of the two facilities are displayed in Fig. 5. HFE-7100 flows in the main loops in both experimental facilities. The main flow loops consist of a reservoir, sub-cooler, micro-gear pump, preheater and test section. A Cole-Parmer micro gear pump (model TW-74014-25) was used in the multi-channels experimental facility, and a Tuthill micro gear pump (model DGS.19EEETNNOM163) was utilised in the single-channel test section experimental set-up. In the single-channel facility, the experimental mass flow rates were measured using Krohne Optimass 3000-S01 Coriolis flow meters mounted to the MFC 300 signal converters. In the multi-channels facility, two Krohne Coriolis flow meters (Optimass 3000-S01 and 3000-S03) were used. An Omega PXM409-007BAI absolute pressure transducer was used to measure the single-channel inlet plenum pressure, whilst an Omega PXM409-001BDWU10V differential pressure transducer was implemented to measure the pressure drop across the single-channel inlet and outlet plena. For the multi-channels inlet pressure and the pressure drop along the heat sink were measured using an Omega PX209-100A5V absolute pressure transducer and an Omega PX409-005DWUI differential pressure transducer, respectively. Finally, K-type thermocouples were utilised for temperature measurement.

Both experimental facilities used a form of condenser after the test section. The condenser was built into the HFE-7100 reservoir tank for

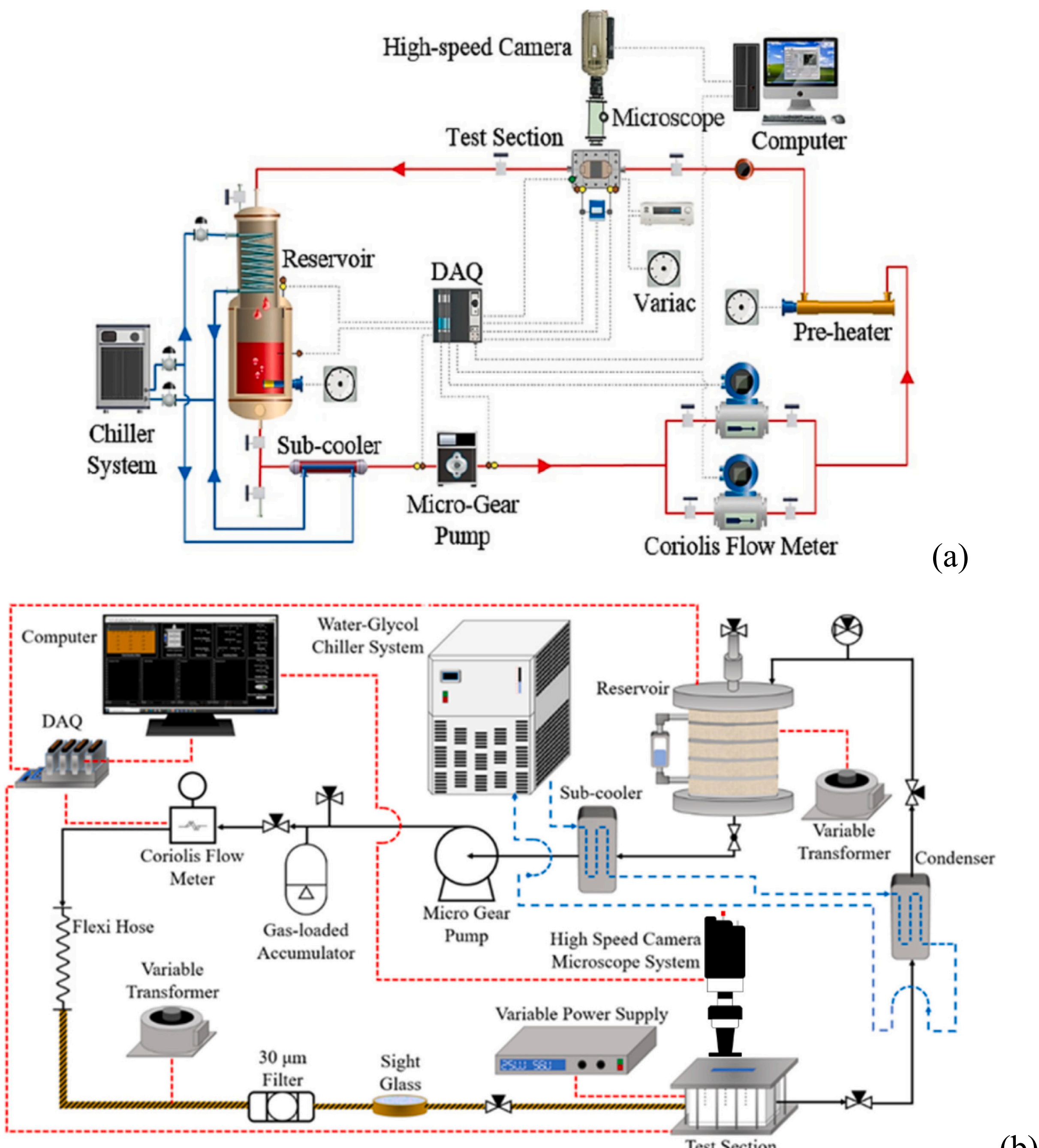

Fig. 5. Schematic of experimental facility: (a) multi-channels, [43], (b) single channel, [44].

the multi-channels experimental facility, whilst a separate condenser and tank were used in the single channel test section. Another slight difference between the two experimental facilities was the use of a gas-loaded accumulator and flexi-hose in the single-microchannel facility, which was used to eliminate undesirable pressure fluctuations resulting from slippage in the pump at the much lower mass flow rates and noise from the Coriolis flow meter. The comparatively larger mass flow rates in the multi-channels heat sink rendered the requirement for such equipment unnecessary. The working fluid was degassed using the reservoir in both experimental facilities, as any dissolved air can significantly alter the heat transfer characteristics of the experiments. The channel inlet pressures were regulated by adjusting the liquid reservoir temperature. Increased channel inlet pressure was achieved by heating the reservoir, using the internal heater in the multi-channels experimental apparatus or an external tape heater in the single-channel facility. Alternatively, the channel inlet pressure was reduced by decreasing the liquid temperature in the reservoir, either by increasing the flow rate to the internal cooling coil in the multi-channels facility or through natural ambient cooling during the single-channel experiments.

The test section design utilised for the multi-channels heat sink experiments is the same as that used in the previous study, which is shown in Fig. 6(a) and is explained extensively in [45]. However, in the present study, the oxygen-free copper microchannel heat sink consisted of thirteen rectangular multi-channels having 1 mm height and 0.95 mm width ($D_h = 0.97$ mm) with a wall thickness of 0.6 mm, covering a base area of 20 mm × 25 mm, see Fig. 6(b). The inlet and outlet plena were designed in a semi-circular shape to ensure uniform flow distribution in these channels. Five thermocouples were inserted horizontally, at 10 mm depth, underneath these channels. These thermocouples were used to enable the heat transfer calculations locally along the heat sink, with the top row of thermocouples location 3.5 mm below the bottom of the channels. The flow entered and exited the manifolds in a vertical direction.

The single-microchannel test section having 30 mm heating length is displayed in Fig. 7(a). The test section had a total height of 30 mm, a base length of 40 mm and a base width of 15 mm as shown in Fig. 7(b). A 10 mm through-hole was drilled into the centre of the 15 mm × 15 mm bottom section of the base to house the 200 W cartridge heater. The upper section of the base that houses the microchannel had a width of 8 mm. The machining parameters used in [44] were replicated to mill the microchannel, plena and O-ring grove. The microchannel was designed with a square-shaped cross section measuring 0.75 mm × 0.75 mm. The average dimensions of the manufactured channel were determined to be a height of 0.814 mm, a width of 0.757 mm ($D_h = 0.784$ mm), and a length of 29.15 mm, using a Zeiss O-Inspect 01–442. These measured values were used in the subsequent data reduction section of this paper. The flow entered and exited vertically to the manifolds. A total of eighteen thermocouple holes were precisely drilled into the front face of the copper base to a depth of 4 mm. This strategic arrangement was designed to evaluate the temperature distribution along the channel and measure both vertical and horizontal heat flux within the copper base. The top row of thermocouples was positioned 1.2 mm beneath the channel's surface in the single-channel test section.

The channel surface roughness parameters were measured using a Bruker NP Flex 3D non-contact, white light optical profiling machine. The average surface roughness, *Ra*, was measured as 0.142 μm and 0.102 μm for the single channel and the multi-channels, respectively, while the average area surface roughness, *Sa*, was measured as 0.138 μm for the single channel and 0.103 μm for the multi-channels. Table 1 shows the experimental operating conditions covered in the present study. The experimental ranges may differ between the single-channel and the multi-channels experiments since different channel geometries and experimental facilities were used. However, for both sets of experiments, the wall heat flux was increased gradually until the dryout region and then the critical heat flux was reached. After that, the input power to the test section was shut down abruptly to prevent thermal failure.

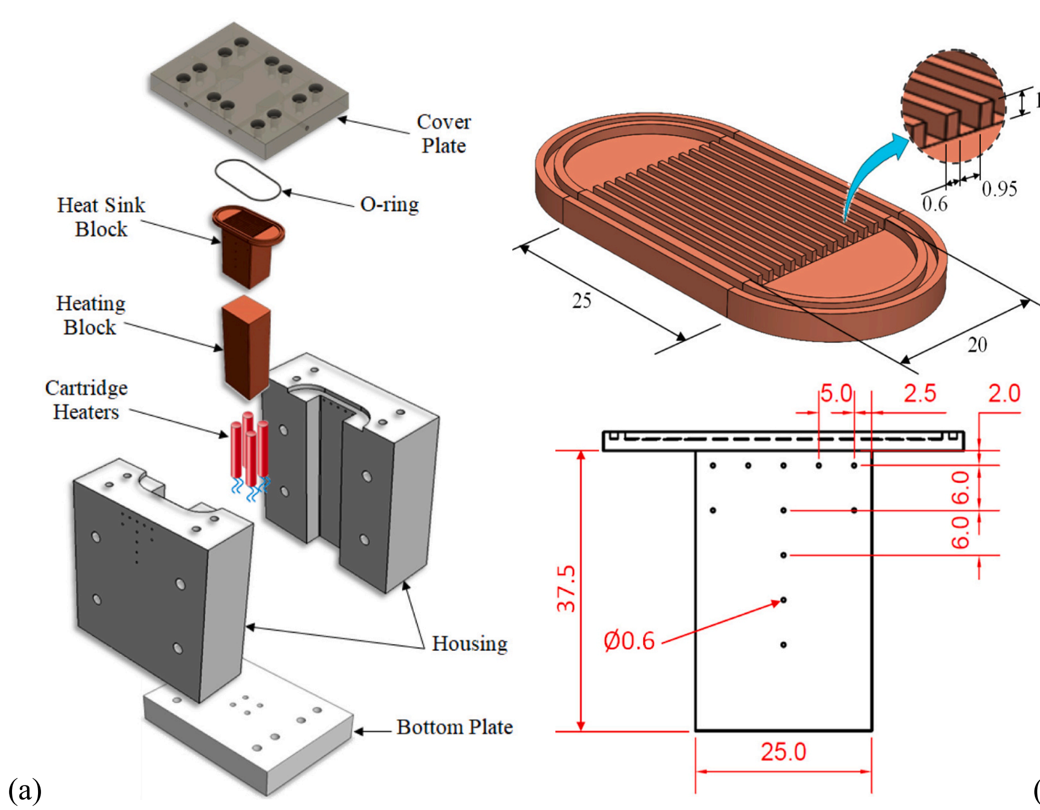

Fig. 6. Multi-channels test section: (a) exploded drawing, [45] (b) heat sink. Dimensions in mm.

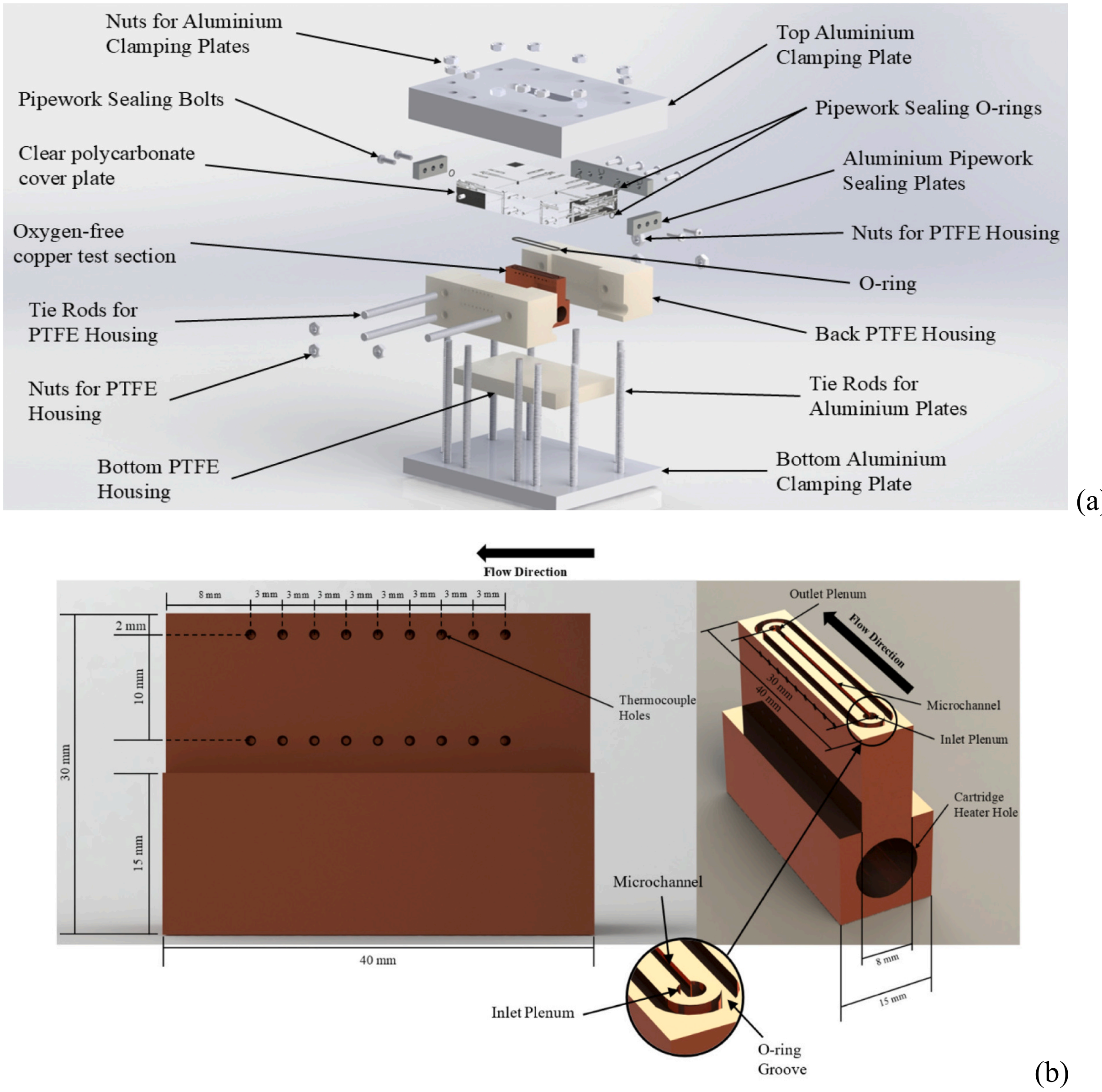

Fig. 7. Single channel test section (a) exploded drawing (b) heat sink.

Table 1
Experimental operating conditions.

For single channel experiments:	
Inlet subcooling	10 K
Inlet pressure	1.5, 2 bar
Mass flux	250–750 kg/m^2 s
Wall heat flux	Up to 435 kW/m^2
Exit vapour quality	Up to 0.71
For multi-channels experiments:	
Inlet subcooling	5 K
Inlet pressure	1, 1.5, 2 bar
Mass flux	100–300 kg/m^2 s
Wall heat flux	Up to 308.6 kW/m^2
Exit vapour quality	Up to 0.97

The thermophysical properties of the working fluid were found from the Engineering Equation Solver (EES) software and presented in Table 2. Three channel different inlet pressures were examined here. The inlet pressure at the test section was controlled via the liquid reservoir. This was carried out by controlling both the cooling process (from the chiller system) and/or heating process (from the immersion heater or the tape heater around this reservoir). HFE-7100 is considered a super-hydrophilic fluid on most surfaces with contact angles of nearly zero, [46]. The measurement of the static contact angle of this fluid was difficult due to complete surface wetting by the fluid droplets, see [47].

2.2. Data reduction

A full detailed data reduction for the multi-channels heat sink experiments is presented in [47]. However, whilst similar to [44] for the single channel, there are some slight variations in the data reduction for the single microchannel experiments. In the single-phase flow experiments, the Fanning friction factor, f_{sp}, for the multi-channels was calculated using Eq. (1).

$$f_{sp} = \frac{\Delta P_{ch} \rho_l D_h}{2 L_{ch} G^2} \tag{1}$$

Pressure measurements, both differential (tapped in both plena) and absolute (tapped in the inlet plenum), were taken from the test section plena. Therefore, the channel pressure drop was obtained from Eq. (2),

Table 2
Thermophysical properties of HFE-7100 at the examined channel inlet pressures.

P_{in} [bar]	T_{sat} [°C]	ρ_l [kg/m^3]	ρ_g [kg/m^3]	ρ_l/ρ_g [−]	i_{lg} [kJ/kg]	μ_l [μPa s]	μ_g [μPa s]	σ [N/m]
1	60.67	1420	9.58	148	115.7	393.7	19.84	0.0096
1.5	73.35	1383	14.13	98	111.3	341.6	20.62	0.0085
2	83.08	1353	18.66	73	107.8	312.2	21.22	0.0077

which considers the change in flow direction in the plena and the pressure drop due to sudden contractions and expansions in the inlet and outlet plena, respectively. Additionally, channel inlet pressures were calculated using Eq. (3). A Consideration of pressure loss components are described in detail in both [44,47].

$$\Delta P_{ch} = \Delta P_{meas} - \left(\Delta P_{in,90} + \Delta P_{sc} + \Delta P_{se} + \Delta P_{out,90}\right) \tag{2}$$

$$P_{in} = \mathrm{P}_{in,meas} - \left(\Delta P_{in,90} + \Delta P_{sc}\right) \tag{3}$$

The mass flux in the multi-channels heat sink was calculated from Eq. (4).

$$G = \frac{\dot{m}}{N_{ch} H_{ch} W_{ch}} \tag{4}$$

The wall heat flux was also calculated assuming a uniform heat flux along the length of the test section. It was also assumed that the top of the test section was adiabatic and that the heat flux in the plenum was negligible. This assumption becomes reasonable for the multi-channels heat sink as: (a) the heat transfer area in the multi-channels is significantly greater than the plenum, and (b) the plena are not located in the copper base. Thus Eq. (5) was used to calculate the wall heat flux in the multi-channels heat sink.

$$q''_w = \frac{q''_b A_b}{(2\eta\, H_{ch} + W_{ch}) L_{ch} N_{ch}} \tag{5}$$

The fin efficiency and the fin parameter are found from Eq. (6) and (7), respectively.

$$\eta = \frac{\tanh(m H_{ch})}{m H_{ch}} \tag{6}$$

$$m = \sqrt{\frac{2h_{(z)}}{k_{cu} W_{fin}}} \tag{7}$$

The base heat flux was calculated using five vertical wall temperature gradients, see Fig. 6(b) to a temperature vs distance relationship, which was then differentiated with distance with the value obtained at y = 0 (bottom surface of the channels) and multiplied by the conductivity of copper, see [47].

$$q''_b = k_{cu} \frac{dT}{dy} \tag{8}$$

The local single-phase heat transfer coefficient was found from Eq. (9).

$$h_{sp(z)} = \frac{q''_w}{T_{w(z)} - T_{f(z)}} \tag{9}$$

The local channel wall temperature, $T_{w(z)}$, was found at each thermocouple location in the top using Eq. (10), where $T_{th(z)}$ represents the measured temperature at the thermocouple location and Δy represents the distance between the thermocouple centre and the channel wall.

$$T_{w(z)} = T_{th(z)} - \frac{q''_b \Delta y}{k_{cu}} \tag{10}$$

The local fluid temperature, $T_{f(z)}$, was found from Eq. (11).

$$T_{f(z)} = T_{in} + \frac{q''_w (2H_{ch} + W_{ch}) z N_{ch}}{\dot{m} c p_l} \tag{11}$$

The average heat transfer coefficient and then the average Nusselt number were found as follows:

$$\overline{h_{sp}} = \frac{1}{L_{ch}} \int_0^{L_{ch}} h_{sp(z)} \tag{12}$$

$$\overline{Nu} = \frac{\overline{h_{sp}} D_h}{k_l} \tag{13}$$

In two-phase flow experiments, the subcooled length L_{sub} could be found using Eq. (14) since two regions (subcooled and saturated regions) occur along the heated length.

$$L_{sub} = \frac{\dot{m} c_{p_l} \left(T_{sat(sub)} - T_{in}\right)}{q''_w (2H_{ch} + W_{ch}) N_{ch}} \tag{14}$$

The saturation temperature at the subcooled length, $T_{sat(sub)}$, reflects the location at which the thermodynamic vapour quality is zero, i.e. the end of the subcooled region. This again was found using the saturation curve from the local pressure, which was determined as follows:

$$P_{sat(sub)} = P_{in} - \frac{2 f_{sp} G^2 L_{sub}}{\rho_l D_h} \tag{15}$$

The friction factor in Eq. (15) was calculated using the correlation proposed by Shah and London [48], which is presented in both [44,47]. As is evident, Eq. (14) is co-dependent with Eq. (15). Therefore, an iterative process was used to determine both the subcooled length and the consequent local saturation pressure. The two-phase pressure drop along the heat sink was found from Eq. (16).

$$\Delta P_{tp} = \Delta P_{ch} - \Delta P_{sp} \tag{16}$$

The local two-phase heat transfer coefficient $h_{tp(z)}$ was calculated from Eq. (8) using $T_{sat(z)}$ instead of $T_{f(z)}$. This local fluid temperature in the saturated region, $T_{sat(z)}$, was obtained from the local pressure, $P_{sat(z)}$, using the saturation curves in the Engineering Equation Solver (EES) software. The local saturation pressure was derived from the following equation:

$$P_{sat(z)} = P_{sat(sub)} - \left(\frac{z - L_{sub}}{L_{ch} - L_{sub}}\right) \Delta P_{tp} \tag{17}$$

The average two-phase heat transfer coefficient was then found by integrating the local two-phase heat transfer coefficients over the two-phase length, see Eq. (18).

$$\overline{h_{tp}} = \frac{1}{L_{ch} - L_{sub}} \int_{L_{sub}}^{L_{ch}} h_{tp(z)} \tag{18}$$

The local vapour quality, defined as the local mass fraction of vapour in the two-phase mixture, was determined through Eq. (19), with $i_{(z)}$ denoting the local specific enthalpy, $i_{l(z)}$ representing the enthalpy of saturated liquid, and $i_{lg(z)}$ signifying the enthalpy of vaporisation.

$$x_{(z)} = \frac{i_{(z)} - i_{l(z)}}{i_{lg(z)}} \tag{19}$$

$$i_{(z)} = i_{in} + \frac{q''_w(2H_{ch} + W_{ch})zN_{ch}}{\dot{m}} \quad (20)$$

It is worth mentioning that these local calculations were carried out at five locations along the multi-channels and nine locations along the single channel heat sink. For the single channel, the same previous procedure was adopted at N_{ch} of one. However, the methodology for calculating the heat flux in this test section differed from that in the multi-channels based on the test section design. The heat flux for each of the thermocouple location seen in Fig. 7(b), q''_{col}, was calculated from the temperature difference between the top and bottom row, dT_{col}, and the distance between the two thermocouple locations, dy, which was 10 mm, as follows:

$$q''_{col} = -k_{cu}\frac{dT_{col}}{dy} \quad (21)$$

A uniform one-dimensional heat flux was assumed in the base of the test section, which was validated by comparing the lowest and largest heat flux of the nine thermocouple columns. The largest difference between the nine columns was found at no point to be larger than 4.2%. The average base heat flux, q''_b, was calculated using Eq. (22).

$$q''_b = \frac{\sum_{i=1}^{9} q''_{col_i}}{9} \quad (22)$$

The wall heat flux, q''_{wall}, was then determined based on the computed base heat flux, assuming a uniform distribution across both the channel and plenum regions. It was calculated using the expression:

$$q''_w = \frac{q''_b A_b - Q_{top}}{(2H_{ch} + W_{ch})L_{ch} + A_{pl_{heat}}} \quad (23)$$

where A_b, $A_{pl_{heat}}$, Q_{top}, H_{ch}, W_{ch} and L_{ch} are the copper base area, the total heated plena area, the heat loss through the top plate, the channel height, the channel width and the channel length, respectively.

An experimentally obtained function for the heat loss through the top plate was found by placing the single-microchannel under vacuum conditions. This was achieved by closing the downstream valve of the single-microchannel test section and attaching a vacuum pump to the test section inlet. Low power heat was then applied to the test section and the base heat flux was calculated using Eq. (22). Under such conditions, it was assumed that all heat applied to the test section was lost through the top plate. The thermal conductance, Υ_{top}, for a given temperature differential between the top surface of the test section and the ambient temperature was then estimated using Eq. (24).

$$q''_b A_b = Q_{top} = \Upsilon_{top}(T_{ts} - T_\infty) \quad (24)$$

The relationship between the thermal conductance through the top plate and the difference between the ambient temperature and the test section top wall is shown in Fig. 8. Data were obtained for two different days with no differences observed.

Both de-gassing and single-phase flow experiments were carried out before conducting two-phase flow experiments. All the measuring instruments were carefully calibrated in the present study. The experimental uncertainties of all variables were calculated using the error propagation methodology proposed by Coleman and Steele [49], which is established from the differential equation presented in Eq. (25). In this equation, X_1, X_2 and X_j represent the measured parameters with the uncertainties of U_{X1}, U_{X2} and U_{Xj}. The combined experimental uncertainties are presented in Table 3.

$$U_r = \sqrt{\left\{\frac{\partial r}{\partial X_1}U_{X1}\right\}^2 + \left\{\frac{\partial r}{\partial X_2}U_{X2}\right\}^2 + \ldots + \left\{\frac{\partial r}{\partial X_j}U_{Xj}\right\}^2} \quad (25)$$

The present data was compared with some existing correlations, and the mean absolute error was used in this comparison as follows:

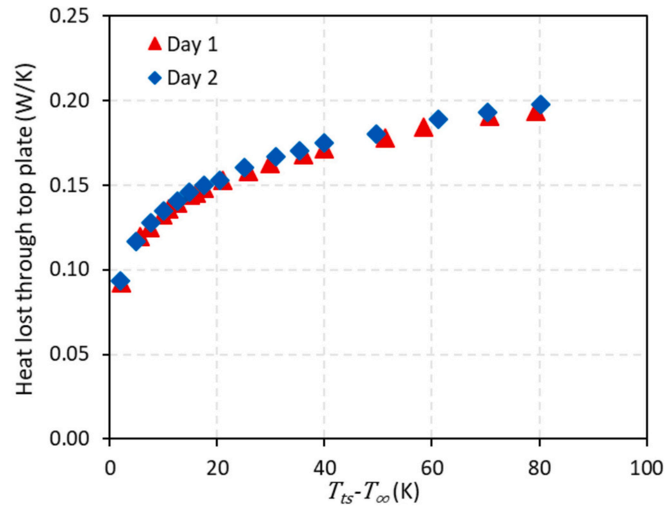

Fig. 8. Experimental thermal conductance through top plate per copper top surface temperature to ambient temperature differential.

Table 3
Experimental uncertainties.

Experimental Parameter	Uncertainty
Inlet temperature	± 0.011–0.22 K
Inlet pressure	± 0.038–0.05 kPa
Differential pressure	± 0.07–0.17%
Mass flux	± 0.2–0.57%
Wall heat flux	± 0.7–16.7%
Fanning friction factor	± 2.44–11.61%
Average Nusselt number	± 4.37–16.5%
Local vapour quality	± 1.2–10.3%
Average two-phase heat transfer coefficient	± 5.31–14.7%

$$MAE = \frac{1}{n}\sum\left|\frac{X_{exp} - X_{pred}}{X_{exp}}\right| \times 100\% \quad (26)$$

where n is the total number of data points.

3. Results and discussion

3.1. Single-phase validations

3.1.1. Single microchannel validation

Single-phase experiments were carried out to ensure the accuracy of the instrumentation and validity of the experimental procedures. Fig. 9 illustrates the experimental Fanning friction factor, f_{sp} from Eq. (1), in adiabatic experiments and the average single-phase Nusselt number, $\overline{Nu}$ from Eq. (13), plotted against the corresponding Reynolds number, Re, respectively. Error bars are included in the figures.

The single-phase friction factor was evaluated against the correlations established by Shah and London [48] for both developing and fully developed laminar flows within rectangular ducts, as shown in Fig. 9(a). The experimental data showed a closer match with the correlation for developing flows, although the results fell between the two correlations. The MAE between the present data and these correlations for developing and developed flows was found to be 22.1% and 36.4%, respectively. Fig. 9(b) compares the single-phase Nusselt number versus Reynolds number with the correlations from Jiang et al. [50] and Lee and Garimella [51]. The experimental results aligned well with these correlations, yielding mean absolute errors of 12.67% and 11.02%, respectively.

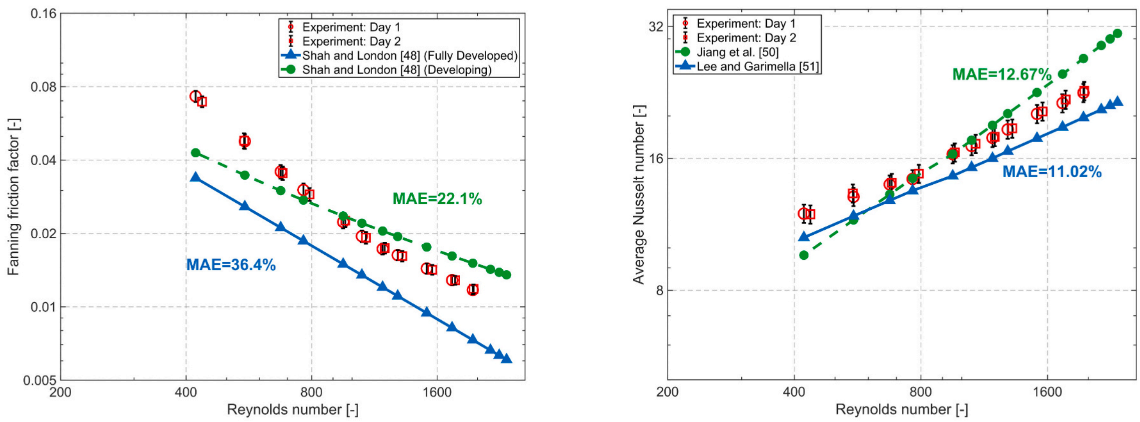

(a) (b)

Fig. 9. Single-phase validation using the single channel heat sink: (a) Fanning friction factor (b) average Nusselt number.

3.1.2. Multi-channels heat sink validation

Fig. 10 depicts the single-phase validation of the multi-channels heat sink compared to past correlations. It is clear from Fig. 10(a) that the correlations by Shah and London [48] for developing flow and Copeland [52] predicted the friction factor results very well with a MAE of 9% and 15%, respectively. The present Nusselt number results are also well predicted by the correlations of Jiang et al. [50] and Lee and Garimella [51] with a MAE of 9% and 23%, respectively, as shown in Fig. 10(b).

The single-phase validation confirmed the accuracy of the instrumentation, and thus the present experimental facilities can be used to carry out high-reliable two-phase flow experiments.

3.2. CHF in a single microchannel

The boiling curves obtained during the experiments using the single microchannel are presented in Fig. 11(a) and (b) for a channel inlet pressure of 1.5 bar and 2 bar, respectively. The effect of channel inlet pressure on the flow boiling curve is presented in Fig. 11(c) for a mass flux of 400 kg/m^2 s. Temperature overshoot (TOS) was detected across all inlet pressures, though its occurrence was inconsistent, showing up sporadically and not across all mass fluxes. A plausible explanation for the absence of TOS might be the accumulation of residual vapour within micro-cavities formed during prior experimental trials.

Fig. 11 shows that wall heat flux demonstrated no significant variation with changes in mass flux from the onset of boiling. This indicated that the largest component mechanism contributing to the two-phase heat transfer was the nucleate boiling mechanism, with smaller contribution from the convective boiling heat transfer mechanism. This phenomenon was noted previously in [43], where nucleation was observed for all observed flow patterns, i.e. for bubbly, slug, churn and annular flows. However, a mass flux effect became apparent as the heat flux is increased towards the dryout region. This mass flux effect in the dryout region is demonstrated in the average two-phase heat transfer coefficients displayed in Fig. 12, which shows that the mass flux delays the dryout region and consequently, achieves higher heat transfer coefficients.

It is important to highlight that the CHF was recorded as the final measured data point before the expected temperature rapid increase, as achieving steady-state conditions at CHF is not feasible due to the high resultant wall temperatures. Furthermore, the applied wall heat flux could only be increased incrementally, making it challenging to approach the true CHF accurately. Nevertheless, a noticeable reduction in the two-phase heat transfer coefficient was observed prior to reaching CHF for nearly all mass fluxes at both channel inlet pressures. Flow visualisation at the outlet for three wall heat fluxes near the CHF helps to explain this phenomenon. This flow visualisation at the channel outlet for the three wall heat fluxes highlighted in Figs. 11 and 12 is presented in Fig. 13.

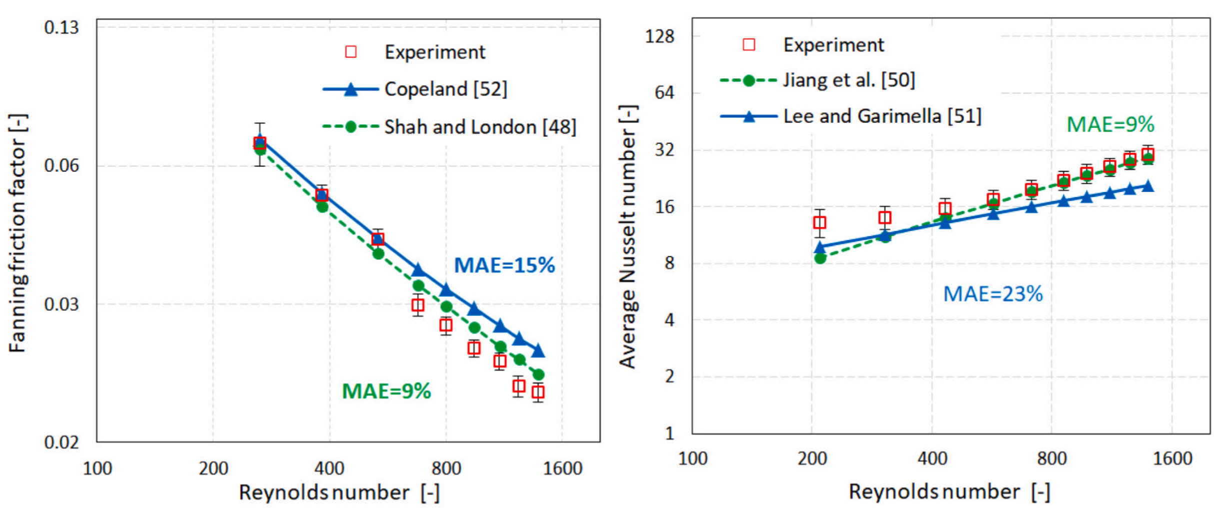

(a) (b)

Fig. 10. Single-phase validation using the multi-channels heat sink: (a) Fanning friction factor (b) average Nusselt number.

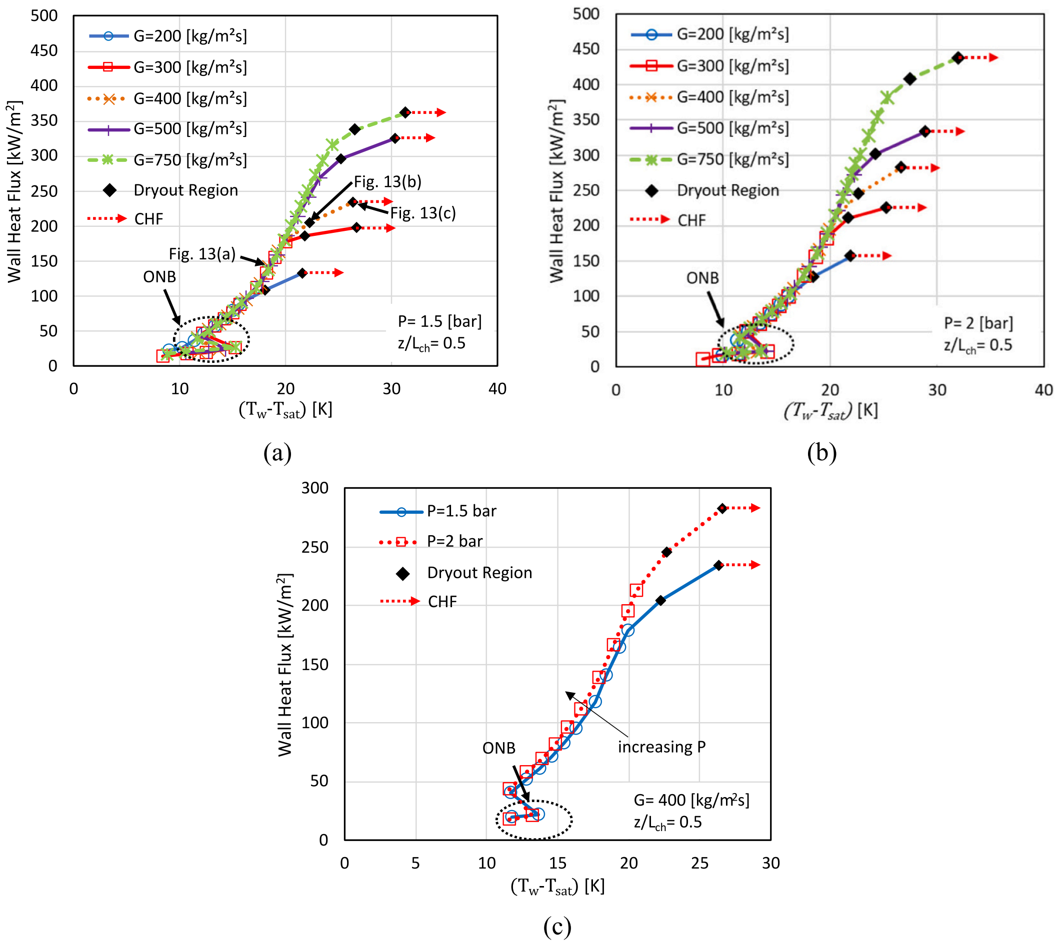

Fig. 11. Boiling curves at z/L = 0.5 for the single channel and inlet pressure of: (a) 1.5 bar (b) 2 bar and (c) the effect of channel inlet pressure. Points indicated refer to flow patterns seen in Fig. 13. (ONB: Onset of Nucleate Boiling).

Fig. 13(a) shows annular flow accompanied by significant bubble nucleation in a thick liquid film at a mass flux of 400 kg/m^2 s and wall heat flux of 140.72 kW/m^2 for a channel inlet pressure of 1.5 bar. There is no evident mass flux effect at this stage, as corroborated by Fig. 12. Although, to be noted, the heat flux value at the occurrence of the CHF increases with mass flux. Fig. 13(b) depicts annular flow with a significantly thinned film at 204.52 kW/m^2, with bubble nucleation no longer present and many dry spots beginning to appear. Despite the absence of nucleation in this region and the appearance of dryout, the two-phase HTC continues to increase with wall heat flux. This is likely due to increased nucleation in the upstream fully wetted section of the channel as a result of the increased wall heat flux.

Finally, Fig. 13(c) presents a fully dried out channel at a wall heat flux of 232.13 kW/m^2; however, this was not a steady state phenomenon. Whilst steady state conditions could not be achieved at CHF, flow visualisation was possible for 1 min from the onset of CHF before the channel wall temperature was sufficiently high that the heating supply to the test section required termination to avoid damage to the experimental facility. This was achievable due to the comparatively low latent heat of vaporisation in comparison to a fluid such as water and the relatively large mass of copper in comparison to the mass flow rate in the channel, resulting in a more gradual but still exponential rise in channel wall temperature. The flow visualisation during the rise of wall temperature at CHF is shown in Fig. 14.

The first image in Fig. 14, taken at $t = 0$ ms, again shows a fully dried out outlet section of the channel, filled entirely with vapour. When this occurred, flow upstream in the channel appeared to come to a complete stop and the inlet pressure begins to rise sharply. This indicated that the vapour in the outlet plenum was 'plugging' the flow, causing a back-pressure and increase in the overall channel pressure. At $t = 1.28$ ms, some condensation began to appear on the clear polycarbonate viewing plate of the test section. This may have either occurred because the now stationary condition of the vapour provided suitable conditions for condensation on the top plate, or the pressure increase in the channel increased the saturation temperature of the fluid. This meant that there was a sufficient differential between the wall temperature of the polycarbonate viewing plate and the saturation temperature of the fluid to result in condensation on the top plate. The mass of vapour condensing was then potentially enough to help 'unplug' the channel outlet, resulting in an onrush of a chaotic mixture of liquid and vapour that can be seen at 6.69 ms. The onrush of liquid then resulted in nucleation at the channel walls, which can be observed at 7.97 ms. The flow then momentarily resembled the annular flow regime at 8.96 ms. The liquid film then begins to reduce in thickness and cause dry spots once more in the channel. These dry spots gradually expand, leading to the complete drying out of the liquid film as seen at $t = 10.68$ ms. Eventually, the channel returns to a fully dry state at 11.22 ms, as observed initially. This periodic dryout behaviour was observed at a wall heat flux of 232.13 kW/m^2. However, the duration of complete outlet dryout at this condition was substantially shorter than that observed during the approach to CHF, which was also momentarily captured through flow visualisation. At 232.13 kW/m^2, the outlet remained fully dried out for 0.823 ms, whereas a dryout duration of 5.12 ms was observed during the wall-temperature rise leading to CHF, for which the instantaneous heat flux could not be quantified. The value of 5.12 ms may have further increased as the wall temperature rose; however, only a short period of

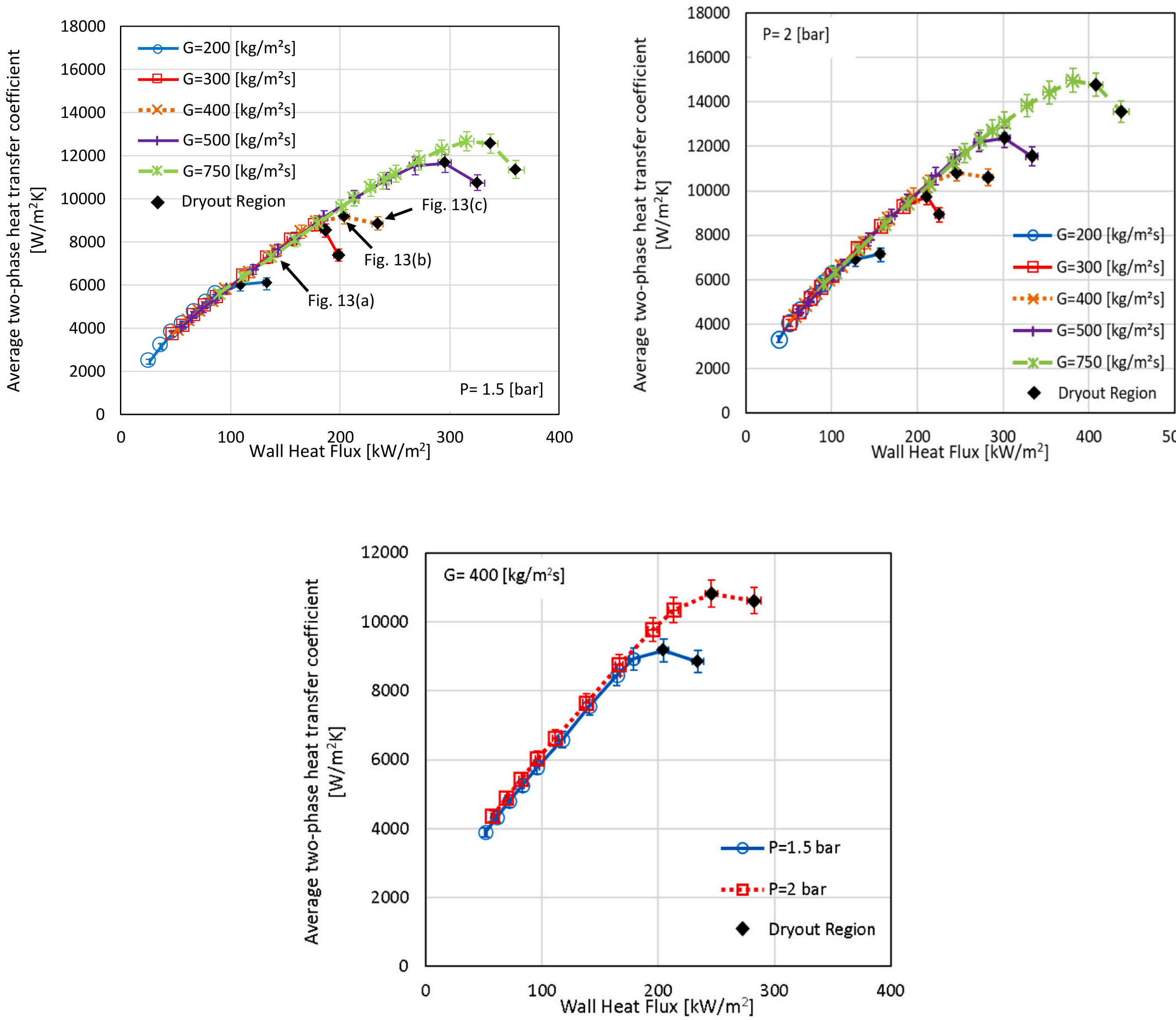

Fig. 12. Average two-phase heat transfer coefficient for the single channel and inlet pressure of: (a) 1.5 bar (b) 2 bar and (c) the effect of channel inlet pressure. Points indicated refer to flow patterns seen in Fig. 13.

flow visualisation was captured.

The frequency of the flow pattern cycle at the channel outlet observed and presented in Fig. 14 may help to explain why steady-state wall temperatures were observed at a heat flux of 234.13 kW/m^2 but not at heat fluxes any higher. The onrush of liquid and consequent nucleation that occurs between 7.97 ms and 10.98 ms likely provides high HTCs; however, the dry out observed will be the cause of the drop in the possible heat transfer rates that causes CHF. It may be that there is the ability for the channel to reach steady-state stable conditions due to the time averaged heat transfer of the flow patterns. However, the system becomes unstable and the period of channel dryout increases exponentially once a certain wall temperature is reached, thus causing the significant rise in wall temperature and ultimately CHF.

The process of the channel becoming ‘plugged’ by the vapour phase in a fully dry channel outlet is linked to the dryout of the annular film. Fig. 11 illustrates that higher CHF values are associated with greater inlet pressures and larger mass fluxes, whilst Fig. 12 shows that the average two-phase HTC also increased with channel inlet pressure. Fig. 15 presents a comparison of annular flow visualisation at the channel outlet between channel inlet pressures, for a mass flux of 400 kg/m^2 s and a heat flux of approximately 200 kW/m^2. This figure shows that dryout spots without clear nucleation occurred on the surface when the inlet pressure was 1.5 bar. In contrast, at 2 bar inlet pressure, the liquid film thickness appears larger with clear nucleation sites, indicating that the thickness is enough to sustain bubble nucleation.

3.3. CHF in multi-microchannels

The effect of wall heat flux, mass flux and inlet pressure on the experimental boiling curve is presented in Fig. 16. This figure shows that the ONB occurred at low wall heat fluxes, i.e. around 10 kW/m^2. A smooth increase in the wall heat flux can be identified here without a temperature overshoot, which was captured in the single channel heat sink. This could be due to the different surface microstructures that are available in a larger active heat transfer area offering different number, sizes and number of cavities for bubble ebullition. Fig. 16(a) depicts that the mass flux effect was insignificant at the low temperature differences of the range studied. A clear dryout region and then CHF were reached at these operating conditions. At the onset of the dryout region, a sudden jump in the surface temperature (ranging from 2.4 to 6 K for the

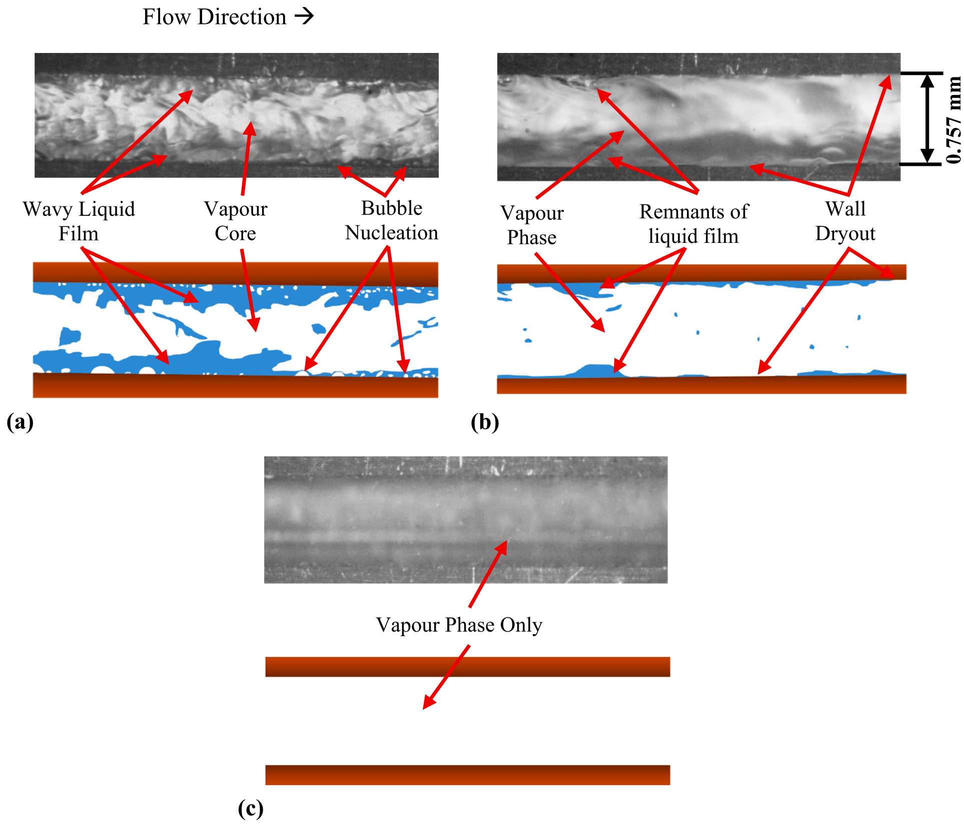

Fig. 13. Flow visualisation and schematic diagram at the single channel outlet for 400 kg/m^2 s mass flux, inlet pressure of 1.5 bar and wall heat fluxes of: (a) 140.72 kW/m^2 (b) 204.52 kW/m^2 (c) 232.13 kW/m^2.

minimum and maximum mass fluxes, respectively) can be identified during these thermal crisis regions. However, the dryout region is considered a stable region, in terms of temperature recorded by the thermocouples embedded in the heat sink (see Fig. 6) while the CHF region showed unstable thermal conditions. As seen in Fig. 17, dryout spots on the heated surface were observed and could eventually occupied most of the surface area and were the cause of the sudden jump in the surface temperature seen in CHF conditions.

A close observation of the flow features depicted in Fig. 17 can allow further examination of flow patterns before and during the dryout region. Annular flow with a vapour core surrounded by a liquid film occurred at the channels outlet at these operating conditions. When the wall heat flux was 242 kW/m^2, some dryout spots were visualized on the surface, see red dashed areas in Fig. 17(a). A complete dry surface can be seen in Fig. 17(b), when the wall heat flux increased to 258 kW/m^2. At these operating conditions, the dryout spots became more and spread on the surface leading to a sudden increase in the surface temperature, mentioned above and seen in Fig. 16.

Fig. 16(b) also shows that increasing inlet pressure led to an increase in the wall heat flux at similar excess temperature values. Smaller bubble departure diameters, higher bubble frequency and higher nucleation site density could be the reason for this enhancement [53]. It can also be seen form Fig. 16 that increasing mass flux resulted in a higher CHF. The CHF was also found to increase, but marginally, with increasing inlet pressure as seen in the figure.

The effect of wall heat flux, mass flux and inlet pressure on the average two-phase heat transfer coefficient is depicted in Fig. 18. It is clear that increasing wall heat flux or inlet pressure led to an increase in the average two-phase heat transfer coefficient. The effect of mass flux was found to be negligible, with the note that higher mass flux results in higher possible CHF values, as explained before. In addition, the dryout region can easily be identified in this figure coinciding with a reduction in the average two-phase heat transfer coefficient during this region.

This increase in the average two-phase heat transfer coefficient and CHF with inlet pressure could be explained using Fig. 19. It can be seen that, at an inlet pressure of 1 bar, annular flow was found at the channels outlet with some dryout spots on the surface, as shown in Fig. 19(a), red dashed areas. In contrast, when the inlet pressure increased to 2 bar, annular flow having a clear liquid film was captured at this location as presented in Fig. 19(b). In addition, several nucleation sites clearly occurred in this liquid film and along the channels.

It can be concluded from the abovementioned results that both wall heat flux and inlet pressure can clearly affect the present two-phase heat transfer coefficient results. In addition, increasing mass flux and inlet pressure results in an increase in the possible CHF values. The effect of pressure on CHF is small compared to the effect of mass flux, i.e. an increase by 6% from 136.5 kW/m^2 to 144.6 kW/m^2 for 1 and 2 bar, respectively. However, an increase in mass flux extends the CHF to higher values, i.e. increasing mass flux from 100 to 300 kg/m^2 s leads to higher CHF by 126% from 136.5 kW/m^2 to 308.6 kW/m^2. This is a significant change and one that designers of thermal management systems should be aware. This could also explain the small pressure effect observed in flow boiling experiments compared to the significant effect seen in pool boiling studies, see for example [54,55]. Inertia force helps remove nucleating bubbles from the heated surface and could reduce this pressure effect.

The recorded CHF in the present multi-channels was found to be significantly higher than that in the single channel heat sink. For example, at a mass flux of 300 kg/m^2 s, the multi-channels provided CHF of 308.6 kW/m^2 at 1 bar, while this value reduced to 198.4 kW/m^2 in the single channel when the inlet pressure was 1.5 bar. This could be attributed to the fact that multi-channels heat sinks have more channels and thus higher mass flow rate is required for a given mass flux leading to increase the supplied heat flux. Dryout of the liquid film in annular

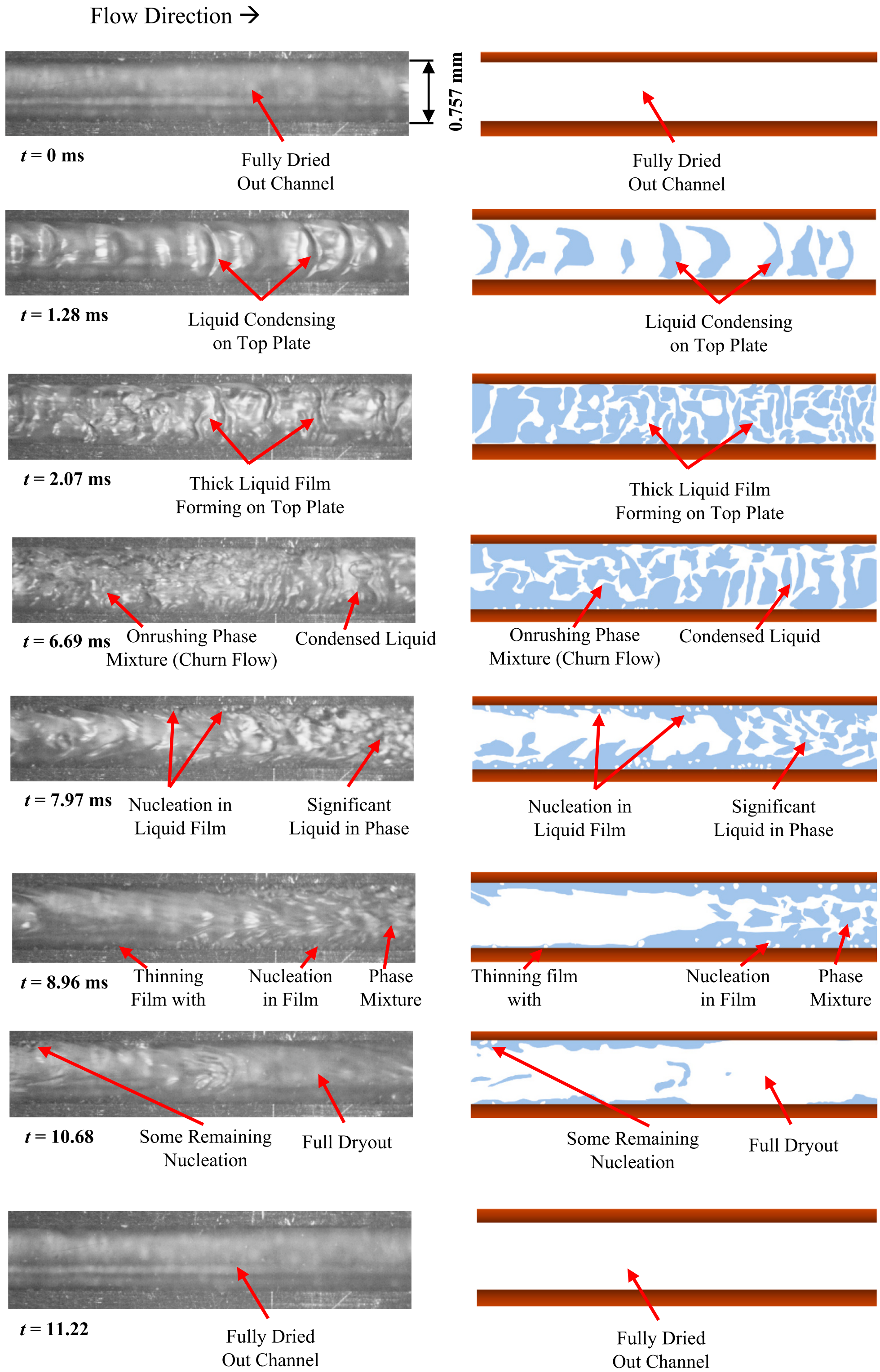

Fig. 14. Flow visualisation at the outlet of the single channel during rise of wall temperature at CHF (after 234.13 kW/m^2) at mass flux of 400 kg/m^2 s and an inlet pressure of 1.5 bar.

flow was identified as the mechanism responsible for CHF in the present heat sinks. The dryout region was found to be the first stage before trigger CHF for the current working fluid. Both mass flux and inlet pressure can affect the occurrence of CHF. It is well-known that higher flow rates enhance liquid replenishment and require larger heat inputs for vapour generation, i.e. higher heat fluxes should be supplied to reach the same vapour quality. This was found to delay the onset of CHF in both heat sinks with increasing mass flux. The effect of inlet pressure on CHF is more complex since this can significantly affect the thermo-physical properties of working fluid, and therefore further assessment is discussed in the next section.

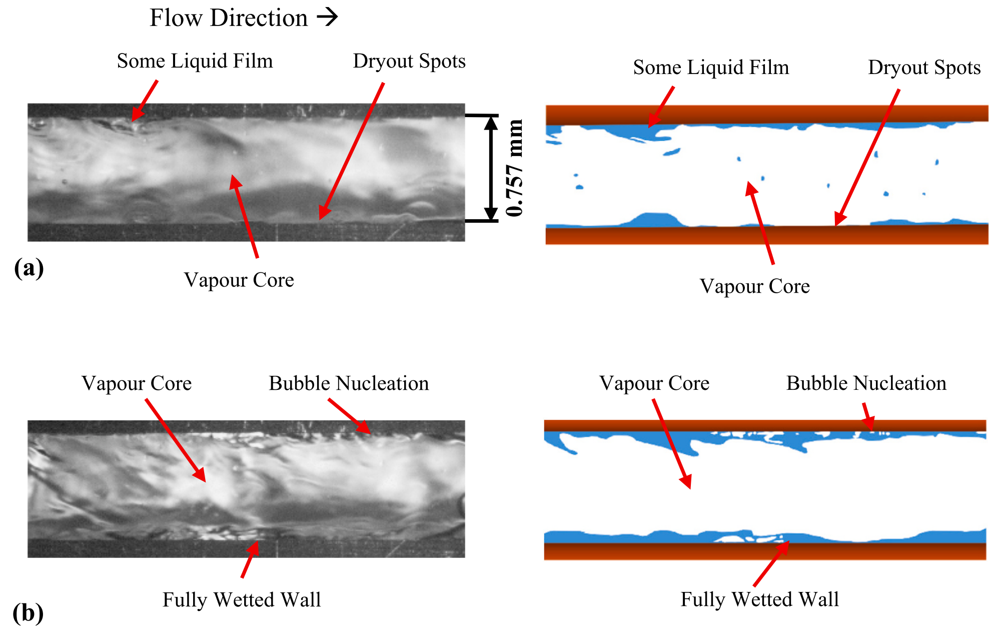

Fig. 15. Outlet annular flow visualisation and schematic diagram for the single channel, 400 kg/m^2 s mass flux and approximately 200 kW/m^2 for inlet pressures of: (a) 1.5 bar (b) 2 bar.

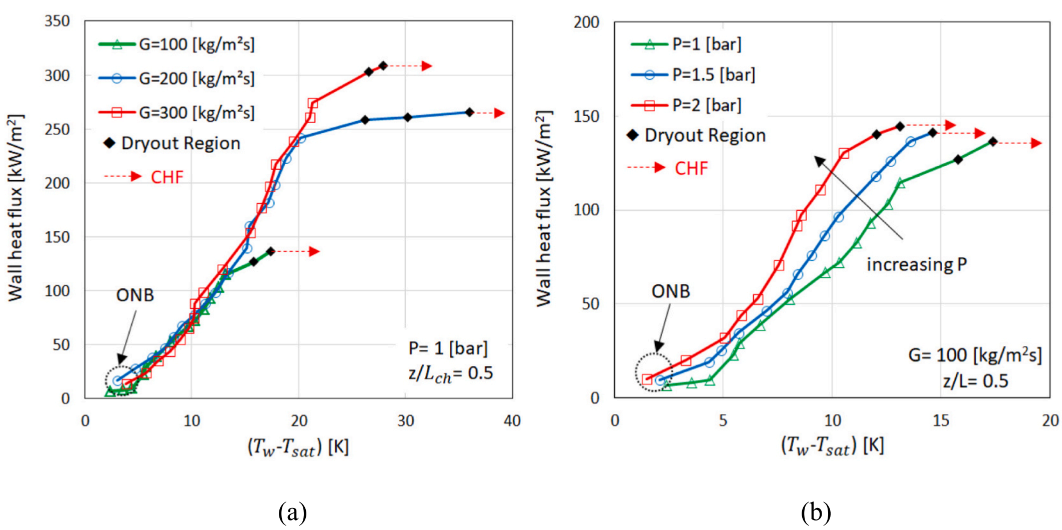

Fig. 16. Boiling curves at z/L = 0.5 for the multi-channels: (a) mass flux effect (b) inlet pressure effect.

3.4. Liquid film thickness – effect of pressure on CHF

It is generally understood that different pressures could result in different liquid film thickness during annular flow. In the literature, there is some disagreement between the effect of increased channel inlet pressure on this thickness for refrigerants in metallic channels, with some researchers reporting thicker film thicknesses [56,57] and others reporting reduced film thicknesses [58]. Different techniques, such as light reflection, high-speed image processing or laser confocal displacement meter, were reported in the literature to measure film thickness during experiments. These methods are wieldy adopted in transparent or metallic tubes having a transparent section at the end. In the present experimental setup (channel with a transparent top-cover plate), it was difficult to accurately measure the thickness of this liquid film. However, an ideal scenario of annular flow with a perfectly circular vapour core is assumed here to estimate the film thickness at the channel corners as shown in Fig. 20. In addition, the interfacial shear stress between the vapour core and the liquid film was calculated since it can affect the film thickness and clarify the effect of pressure.

The liquid film thickness at the corners was found from Eq. (27).

$$\delta = \sqrt{\left(\frac{H_{ch}}{2}\right)^2 + \left(\frac{W_{ch}}{2}\right)^2} - r \tag{27}$$

The radius of vapour core r was calculated from the void fraction since the ratio of cross-sectional area occupied by the vapour phase to the cross-sectional area of the entire channel is expressed by the void fraction [59].

$$\alpha = \frac{A_g}{A_{sec}} \tag{28}$$

$$A_g = \pi r^2 \tag{29}$$

The void fraction correlation proposed by Zivi [60] was used in this analysis as shown in Eq. (30).

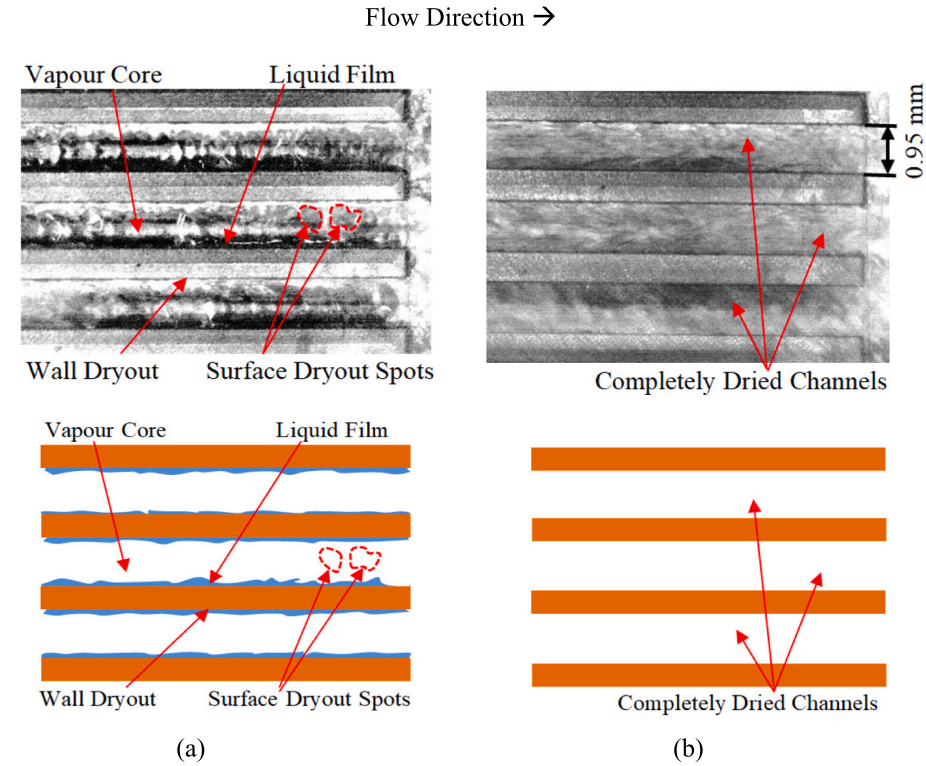

Fig. 17. Outlet annular flow visualisation and schematic diagram for the multi-channels, before and during the dryout region at 1 bar inlet pressure, 200 kg/m^2 s mass flux and wall heat flux of: (a) 242 kW/m^2 (before dryout) (b) 258 kW/m^2 (during dryout).

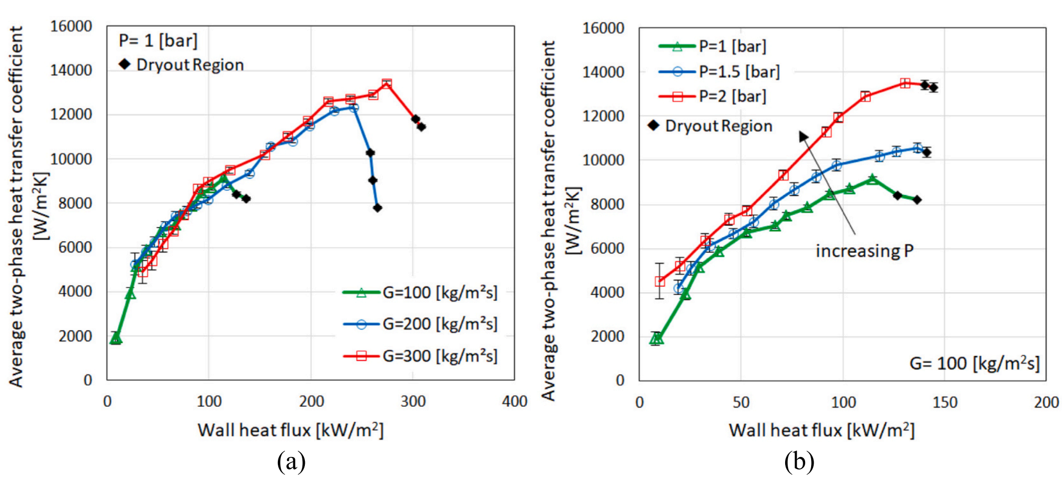

Fig. 18. Average two-phase heat transfer coefficient for the multi-channels: (a) mass flux effect (b) inlet pressure effect.

$$\alpha = \left[1 + \frac{1-x}{x}\left(\frac{\rho_g}{\rho_l}\right)^{0.67}\right]^{-1} \tag{30}$$

The interfacial shear stress was calculated using the method described by Patel et al. [61].

$$\tau_i = \frac{1}{2}\rho_g f_i u_g^2 \tag{31}$$

$$u_g = \frac{\dot{m}_g}{\rho_g A_g} \tag{32}$$

$$\dot{m}_g = xGA_{sec} \tag{33}$$

The interface friction factor f_i was found from the correlation developed by Moeck [62] for annular flow as follows:

$$f_i = 0.005\left[1 + 1458\left(\frac{\delta}{D_h}\right)^{1.42}\right] \tag{34}$$

Fig. 21 depicts both liquid film thickness and interfacial shear stress at two different inlet pressures. This figure was plotted for a single channel having height and width of 0.75 × 0.75 mm, length of 30 mm, mass flux of 400 kg/m^2 s, inlet sub-cooling of 10 K and heat flux up to 300 kW/m^2.

The figure shows that the liquid film thickness decreases with increasing heat flux, and consequently vapour quality, as expected. In contrast, increasing heat flux leads to increase the interfacial shear stress due to the higher vapour superficial velocity. Fig. 21 also presents that increasing inlet pressure from 1 to 2 bar can result in a reduction in the

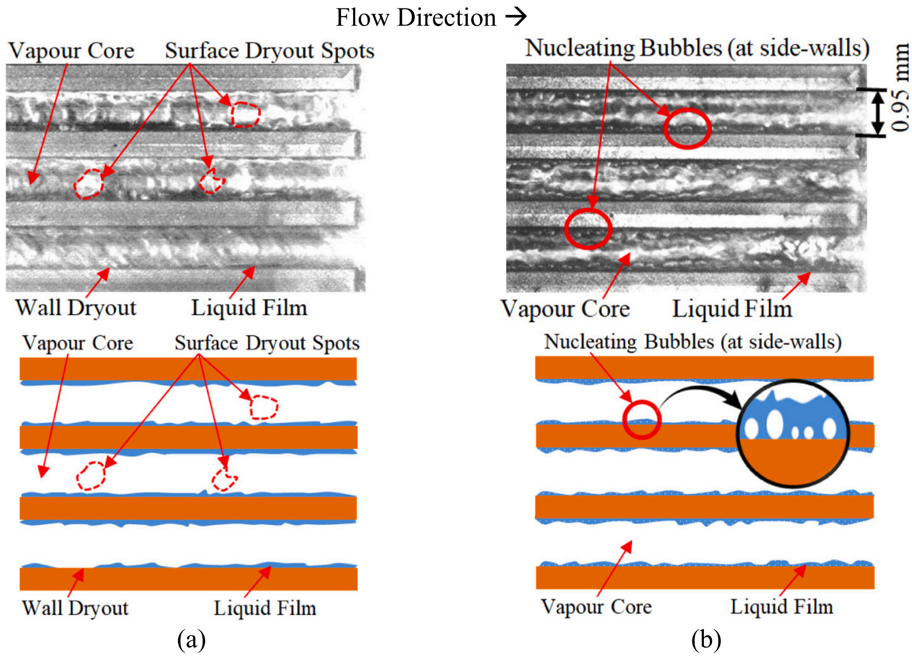

Fig. 19. Outlet annular flow visualisation and schematic diagram for the multi-channels, 100 kg/m^2 s mass flux and approximately 114 kW/m^2 wall heat flux for inlet pressure of: (a) 1 bar and (b) 2 bar.

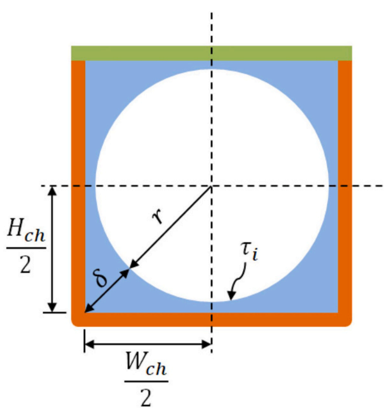

Fig. 20. Idealised scenario of annular flow with perfectly circular vapour core cross-section.

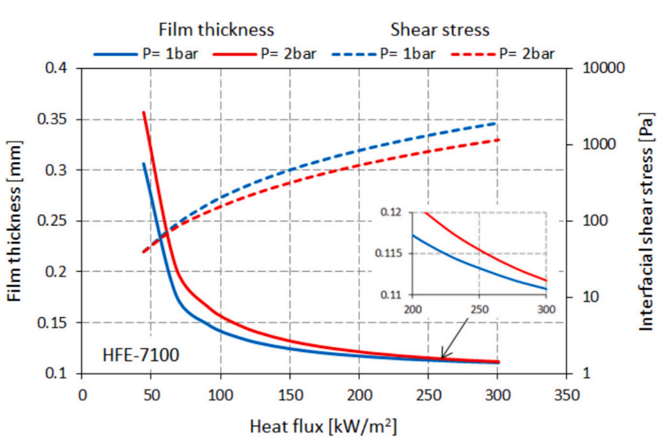

Fig. 21. Liquid film thickness and interfacial shear stress of idealised scenario of annular flow.

interfacial shear stress and thicker liquid film. It is well-known that fluid thermophysical properties can vary with pressure. Increasing inlet pressure from 1 to 2 bar reduces the density ratio by 51% and the latent heat of vaporisation by only 7% as presented in Table 2. Reducing this density ratio results in a reduction in the vapour superficial velocity, and thus a small amount of liquid is removed from the surface as a result of low interfacial shear stress. Accordingly, thicker liquid film is expected to form on the heated surface with increasing pressure. This thick liquid film could delay the appearance of dryout areas and then CHF, while also enhancing the nucleation process during annular flow as shown in the present flow visualisation results. Higher pressure results in smaller nucleating bubbles, [53], and then nucleation is more likely to occur in a thick liquid film.

3.5. *CHF comparison to existing correlations*

3.5.1. *Single channel*

Fig. 22 presents a comparison of the newly obtained experimental results for a single microchannel with eight established CHF prediction correlations developed, for small-micro passages covering 0.2–7 mm channel size, in the form of thermal maps. The eight correlations are presented in Appendix A. The thermal map represents all data points for the single-microchannel depicting the CHF point, shown in black. The data points for which dryout begin to occur are shown in orange. The data plotted in green symbols are for heat flux values below these two conditions and represent safe operational margins for the heat sink used in a thermal management system, i.e. avoiding CHF with possible catastrophic system failure. A summary of the CHF results for the single-channel experiments is also presented in Table 4.

In the current study, the correlation by Bowers and Mudawar [34] was applied to the new experimental data and its accuracy evaluated. This correlation over-predicted the present results with a combined MAE of 45% for both channel inlet pressures. The correlation by Qu and Mudawar [16] performed poorly when compared to the current study, substantially over-predicting CHF across all conditions. The combined mean absolute error of this correlation was found to be 216%. The correlation by Kuan [35] exhibited also poor performance, with a combined MAE of 93%. Another poor prediction was found when the

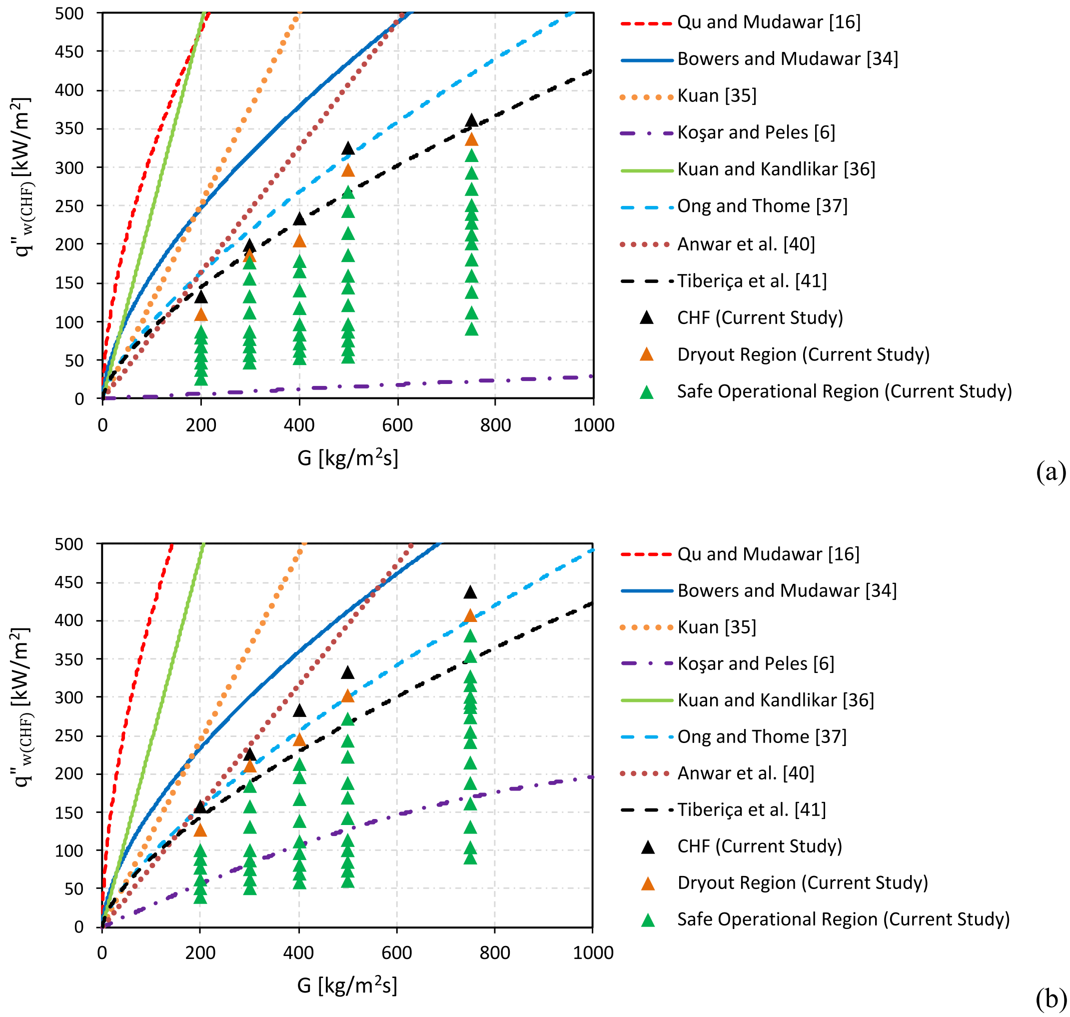

Fig. 22. Comparison between CHF prediction tools and the single channel CHF results for inlet pressure of: (a) 1.5 bar (b) 2 bar.

Table 4
Critical heat flux results for single-channel experiments.

Channel Inlet Pressure [bar]	Channel Inlet Subcooling [K]	Mass Flux [kg/ m^2 s]	Outlet Vapour Quality [−]	Critical Heat Flux [kW/ m^2]
1.5	10	200	0.5702	132.676
1.5	10	300	0.5356	198.35
1.5	10	400	0.4999	234.13
1.5	10	500	0.6032	325.36
1.5	10	750	0.4324	360.70
2	10	200	0.72	157.06
2	10	300	0.6877	225.54
2	10	400	0.6424	282.48
2	10	500	0.6278	333.62
2	10	750	0.5423	437.59

correlation by Kuan and Kandlikar [36] was assessed here. Their correlation over-predicted our CHF data with a combined MAE of 305%. The CHF correlation by Koşar and Peles [6] under-predicted the experimental data with a combined MAE of 79%. In contrast to the poor predictions of the previous correlations, the following correlations predicted the present results more accurately. For example, the correlations by Ong and Thome [37] showed a MAEs of 10% and similarly the correlation by Tibiriça et al. [41] demonstrated a strong predictive performance when applied to the current dataset, producing a combined MAE of 12%.

3.5.2. Multi-channels

Fig. 23 shows the evaluation of the same eight existing CHF correlations using the present experimental results of the multi-channels heat sink, whilst the CHF results are summarised in Table 5. Fig. 23(a) presents the effect of mass flux on the CHF. Although all the proposed correlations showed a clear increase in CHF with increasing mass flux, a large discrepancy can be seen among them. Some of these correlations over or under-predicted the present data with a MAE more than 50%, such as Koşar and Peles [6], Qu and Mudawar [16] and Kuan and Kandlikar [36]. The under-prediction by [6] could be due to the empirical constants used in their correlation based on their results, see Appendix A. These empirical constants result in lower values predicted by their correlation, when compared to the present results. The noticeable over-prediction by [16,36] could be due to the fact that these correlations were proposed based on limited number of data, where water is the common working fluid. The different fluid properties, such as high latent heat of evaporation compared to HFE-7100, could result in this over-prediction. In contrast, a good agreement was found with the correlations by Bowers and Mudawar [34], Kuan [35], Ong and Thome [37], Anwar et al. [40] and Tibiriça et al. [41]. These correlations provided a MAE equal or less than 20%. It is interesting to see that the correlation by Tibiriça et al. [41] showed the best agreement, with minimum mean absolute error of 7.4%.

The effect of different inlet pressures on CHF is presented in Fig. 23 (b). Only six correlations [6,35–37,40,41], were presented in this figure since different ranges of channel inlet pressure were covered in these

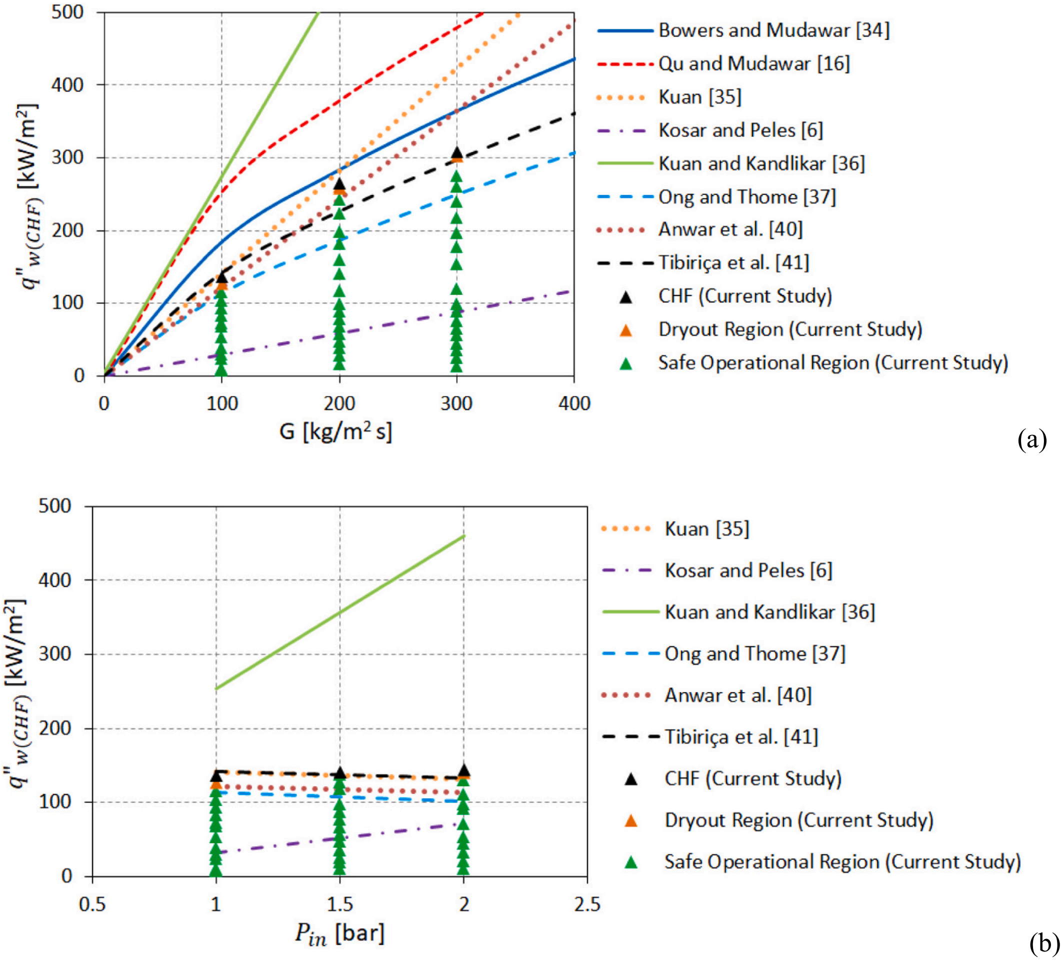

Fig. 23. Comparison between CHF prediction tools and the multi-channels CHF results:

Table 5
Critical heat flux results for multi-channels experiments.

Channel Inlet Pressure [bar]	Channel Inlet Subcooling [K]	Mass Flux [kg/m^2 s]	Outlet Vapour Quality [−]	Critical Heat Flux [kW/m^2]
1	5	100	0.87	136.5
1	5	200	0.9	265.5
1	5	300	0.64	308.6
1.5	5	100	0.97	141.3
2	5	100	0.96	144.6

studies. Two different trends can be identified in this figure. The first group shows a marginal reduction in CHF with increasing inlet pressure. This group includes the correlations proposed by Kuan [35], Ong and Thome [37], Anwar et al. [40] and Tibiriça et al. [41]. In contrast, the second group shows that increasing inlet pressure can lead to an increase in the CHF, see Koşar and Peles [6] and the more drastic increases in the work of Kuan and Kandlikar [36].

(a) mass flux effect at 1 bar inlet pressure (b) inlet pressure effect at 100 kg/m^2 s mass flux.

The above comparison of both heat sinks shows that possible different CHF mechanisms, operating conditions, length-to-diameter ratios and fluid properties can significantly affect the prediction of the CHF in micro passages proposed by past correlations. For example, the correlations by [16,34], covered very high inlet subcooling of 10–70 K. In addition, the correlation by Qu and Mudawar [16] was proposed for CHF mechanism due to flow reversal, which differs from what was found in the present study. The observation of an entirely different CHF mechanism is likely the reason for the significantly different prediction of the CHF observed in this study. The use of the receding contact angle in the correlation by [36] has a noticeable effect on its predictive accuracy. The measurement of this angle could be more challenging, especially with super-hydrophilic fluids that have high evaporation rates. Heated length is another key control parameter that significantly influences CHF.

Long channel lengths of 63.5 mm and 213–245 mm covered in the studies by [35,40] could limit the prediction of these correlations compared to the present heated lengths of 25 and 30 mm. Although the correlation proposed by Koşar and Peles [6] captures the pressure-dependent trend, it shows a noticeable disagreement with the present results. This could be due to the fact that their correlation was proposed specifically for only one working fluid (R-123) and this pressure-property relationship obtained for this refrigerant does not generalize well to HFE-7100. The short heated length of 10 mm used in their study may be another factor contributing to this discrepancy. The present comparison shows that the correlations by Ong and Thome [37] and Tibiriça et al. [41] show the best prediction compared to others. The use of different working fluids in these studies, covering a wide range of operating conditions and channel length-to-diameter ratios, could have enhanced the accuracy of their predictions. However, the present experimental pressure-dependent trend was not exactly captured by these correlations. These correlations show a decreasing trend with increasing pressure, which contrasts with the present results. The assessment of existing correlations confirms the significant influence of mass flux on CHF. The effect of inlet pressure is still complex, resulting in noticeable discrepancies among the evaluated correlations.

4. Conclusions

Flow boiling critical heat flux of HFE-7100 in single and multi-channels heat sinks was experimentally examined in this paper. The present two-phase flow experiments were carried out at 1–2 bar inlet pressure, 5 K and 10 K inlet subcooling and mass flux ranging from 100 to 750 kg/m^2 s. A high-speed, high-resolution camera was also used to capture the features of flow patterns, and help further understanding of the CHF phenomenon. Maximum wall heat fluxes of 435 kW/m^2 and 308.6 kW/m^2 were reached in the single channel and the multi-channel heat sinks, respectively. The heat transfer results showed that the average two-phase heat transfer coefficient increased with increasing wall heat flux in both heat sinks. Increasing the mass flux leads to higher critical heat flux levels, this then being one method that can be used to achieve higher operational limits on microchannels employed in cooling electronic components. Higher inlet pressure has also resulted in an increase of the possible critical heat flux values, but this effect is only marginal. This could be due to changes in the liquid-to-vapour density ratio.

The CHF mechanism under the experimental conditions of the present study was attributed to the liquid film dryout during annular flow. This caused the surface temperature to increase rapidly leading to a reduction in the heat transfer coefficient rates. The present CHF results were predicted very well by the correlation proposed by Tibiriça et al. [41] for both the single and multi-channels heat sinks. It can therefore be recommended for design purposes. It is worth noting however, the pressure-dependent trend was not captured well by any of the correlations indicating the complex effect of inlet pressure on CHF behaviour. This is recommended for further study, especially if pressures higher that 2 bar will be reached.

Declaration of competing interest

The authors declare that they have no known competing financial interests or personal relationships that could have appeared to influence the work reported in this paper.

Acknowledgements

The work was conducted with the support of the Engineering and Physical Sciences Research Council of the UK, under Grant: EP/T033045/1.

The authors would also like to thank Mr. Costas Xanthos for his help in the design and construction of the experimental facilities.

Data availability

Data will be made available on request.

References

[1] L. Tan, P. Liu, C. She, P. Xu, L. Yan, H. Quan, Heat dissipation characteristics of IGBT module based on flow-solid coupling, Micromachines 2022, Vol. 13, Page 554 13 (2022) 554. Doi: https://doi.org/10.3390/MI13040554.
[2] C. Qian, A.M. Gheitaghy, J. Fan, H. Tang, B. Sun, H. Ye, G. Zhang, Thermal management on IGBT power electronic devices and modules, IEEE Access 6 (2018) 12868–12884, https://doi.org/10.1109/ACCESS.2018.2793300.
[3] I. Mudawar, Assessment of high-heat-flux thermal management schemes, IEEE Transactions on Components and Packaging Technologies 24 (2001) 122–141, https://doi.org/10.1109/6144.926375.
[4] S.G. Kandlikar, A.V. Bapat, Evaluation of jet impingement, spray and microchannel chip cooling options for high heat flux removal, Heat Transf. Eng. 28 (2007) 911–923, https://doi.org/10.1080/01457630701421703;REQUESTEDJOURNAL:JOURNAL:UHTE20;PAGE:STRING:ARTICLE/CHAPTER.
[5] Z. Zhang, X. Wang, Y. Yan, A review of the state-of-the-art in electronic cooling, E-Prime - Advances in Electrical Engineering, Electronics and Energy 1 (2021) 100009, https://doi.org/10.1016/J.PRIME.2021.100009.
[6] A. Koşar, Y. Peles, Critical heat flux of R-123 in silicon-based microchannels, J. Heat Transfer 129 (2007) 844–851, https://doi.org/10.1115/1.2712852.
[7] R. Mastrullo, A.W. Mauro, J.R. Thome, G.P. Vanoli, L. Viscito, Critical heat flux: performance of R1234yf, R1234ze and R134a in an aluminum multi-minichannel heat sink at high saturation temperatures, Int. J. Therm. Sci. 106 (2016) 1–17, https://doi.org/10.1016/J.IJTHERMALSCI.2016.03.011.
[8] B. Parizad Benam, A.K. Sadaghiani, V. Yağcı, M. Parlak, K. Sefiane, A. Koşar, Review on high heat flux flow boiling of refrigerants and water for electronics cooling, Int. J. Heat Mass Transf. 180 (2021) 121787, https://doi.org/10.1016/J.IJHEATMASSTRANSFER.2021.121787.
[9] T.G. Karayiannis, M.M. Mahmoud, Flow boiling in microchannels: fundamentals and applications, Appl. Therm. Eng. 115 (2017) 1372–1397, https://doi.org/10.1016/J.APPLTHERMALENG.2016.08.063.
[10] Y. Katto, Critical heat flux, Adv. Heat Transf. 17 (1985) 1–64, https://doi.org/10.1016/S0065-2717(08)70284-3.
[11] S.M. Kim, I. Mudawar, Review of databases and predictive methods for heat transfer in condensing and boiling mini/micro-channel flows, Int. J. Heat Mass Transf. 77 (2014) 627–652, https://doi.org/10.1016/J.IJHEATMASSTRANSFER.2014.05.036.
[12] G. Liang, I. Mudawar, Review of spray cooling – part 1: single-phase and nucleate boiling regimes, and critical heat flux, Int. J. Heat Mass Transf. 115 (2017) 1174–1205, https://doi.org/10.1016/J.IJHEATMASSTRANSFER.2017.06.029.
[13] N. Mascarenhas, I. Mudawar, Analytical and computational methodology for modeling spray quenching of solid alloy cylinders, Int. J. Heat Mass Transf. 53 (2010) 5871–5883, https://doi.org/10.1016/J.IJHEATMASSTRANSFER.2010.06.055.
[14] G. Liang, I. Mudawar, Pool boiling critical heat flux (CHF) – part 1: review of mechanisms, models, and correlations, Int. J. Heat Mass Transf. 117 (2018) 1352–1367, https://doi.org/10.1016/J.IJHEATMASSTRANSFER.2017.09.134.
[15] L. Guo, J. Camm, T. Hirokawa, H. Li, L. Huang, A detailed review on the role of critical heat flux in micro-channel dryout phenomena and strategies for heat transfer enhancement, Int. J. Heat Mass Transf. 241 (2025) 126740, https://doi.org/10.1016/J.IJHEATMASSTRANSFER.2025.126740.
[16] W. Qu, I. Mudawar, Measurement and correlation of critical heat flux in two-phase micro-channel heat sinks, Int. J. Heat Mass Transf. 47 (2004) 2045–2059, https://doi.org/10.1016/J.IJHEATMASSTRANSFER.2003.12.006.
[17] S.M. Kim, I. Mudawar, Thermal design and operational limits of two-phase micro-channel heat sinks, Int. J. Heat Mass Transf. 106 (2017) 861–876, https://doi.org/10.1016/J.IJHEATMASSTRANSFER.2016.10.020.
[18] H. Zhang, I. Mudawar, M.M. Hasan, Flow boiling CHF in microgravity, Int. J. Heat Mass Transf. 48 (2005) 3107–3118, https://doi.org/10.1016/J.IJHEATMASSTRANSFER.2005.02.015.
[19] D.D. Hall, I. Mudawar, Ultra-high critical heat flux (CHF) for subcooled water flow boiling—II: high-CHF database and design equations, Int. J. Heat Mass Transf. 42 (1999) 1429–1456, https://doi.org/10.1016/S0017-9310(98)00242-7.
[20] T.C. Willingham, I. Mudawar, Forced-convection boiling and critical heat flux from a linear array of discrete heat sources, Int. J. Heat Mass Transf. 35 (1992) 2879–2890, https://doi.org/10.1016/0017-9310(92)90308-F.
[21] J.C. Sturgis, I. Mudawar, Critical heat flux in a long, rectangular channel subjected to one-sided heating—II. Analysis of critical heat flux data, Int. J. Heat Mass Transf. 42 (1999) 1849–1862, https://doi.org/10.1016/S0017-9310(98)00275-0.
[22] W. Liu, S. Peng, G. Jiang, Y. Liu, Development and assessment of a new CHF mechanistic model for subcooled and low quality flow boiling, Int. J. Heat Mass Transf. 165 (2021) 120641, https://doi.org/10.1016/J.IJHEATMASSTRANSFER.2020.120641.
[23] M. Yan, Q. He, Z. Ma, H. Liu, L. Wan, Z. Li, L. ming Pan, Experimental investigation and a mechanical model of critical heat flux in a narrow rectangular channel, Exp. Therm. Fluid Sci. 128 (2021) 110432, https://doi.org/10.1016/J.EXPTHERMFLUSCI.2021.110432.
[24] J. Weisman, B.S. Pei, Prediction of critical heat flux in flow boiling at low qualities, Int. J. Heat Mass Transf. 26 (1983) 1463–1477, https://doi.org/10.1016/S0017-9310(83)80047-7.
[25] S.S. Kutateladze, A.I. Leont'ev, Some Applications of the Asymptotic Theory of the Turbulent Boundary Layer, in: Proceedings of the Third International Heat Transfer Conference, New York, 1966.
[26] C.H. Lee, I. Mudawwar, A mechanistic critical heat flux model for subcooled flow boiling based on local bulk flow conditions, International Journal of Multiphase Flow 14 (1988) 711–728, https://doi.org/10.1016/0301-9322(88)90070-5.
[27] J.G. Kirby, R. Stainforth, L.H. Kinnier, A Visual Study of Forced Convective Boiling. Part II: Flow patterns and burnout for a round test section, 1967.
[28] L.S. Tong, G.F. Hewitt, Overall Viewpoint of Flow Boiling CHF Mechanisms, 1972.
[29] W.X. Liu, W.X. Tian, Y.W. Wu, G.H. Su, S.Z. Qiu, X. Yan, Y.P. Huang, D.X. Du, An improved mechanistic critical heat flux model and its application to motion conditions, Prog. Nucl. Energy 61 (2012) 88–101, https://doi.org/10.1016/J.PNUCENE.2012.07.002.
[30] J. Lee, I. Mudawar, Critical heat flux for subcooled flow boiling in micro-channel heat sinks, Int. J. Heat Mass Transf. 52 (2009) 3341–3352, https://doi.org/10.1016/J.IJHEATMASSTRANSFER.2008.12.019.
[31] H.S. Ahn, S.H. Kang, C. Lee, J. Kim, M.H. Kim, The effect of liquid spreading due to micro-structures of flow boiling critical heat flux, Int. J. Multiphase Flow 43 (2012) 1–12, https://doi.org/10.1016/J.IJMULTIPHASEFLOW.2012.02.003.
[32] G.F. Hewitt, Liquid-Gas Systems, in: G. Hetsroni (Ed.), Handbook of Multiphase Systems, Hemisphere, Washington, D.C., 1982.

[33] V.Y.S. Lee, T.G. Karayiannis, Effect of inlet subcooling on flow boiling in microchannels, Appl. Therm. Eng. 181 (2020) 115966, https://doi.org/10.1016/j.applthermaleng.2020.115966.
[34] M.B. Bowers, I. Mudawar, High flux boiling in low flow rate, low pressure drop mini-channel and micro-channel heat sinks, Int. J. Heat Mass Transf. 37 (1994) 321–332, https://doi.org/10.1016/0017-9310(94)90103-1.
[35] W.K. Kuan, Experimental Study of Flow Boiling Heat Transfer and Critical Heat Flux in Microchannels, Rochester Institute of Technology, 2006. ://repository.rit.edu/theses (accessed February 9, 2025).
[36] W.K. Kuan, S.G. Kandlikar, Experimental study and model on critical heat flux of refrigerant-123 and water in microchannels, J. Heat Transfer 130 (2008), https://doi.org/10.1115/1.2804936/475427.
[37] C.L. Ong, J.R. Thome, Macro-to-microchannel transition in two-phase flow: part 2 – flow boiling heat transfer and critical heat flux, Exp. Therm. Fluid Sci. 35 (2011) 873–886, https://doi.org/10.1016/J.EXPTHERMFLUSCI.2010.12.003.
[38] L. Wojtan, R. Revellin, J.R. Thome, Investigation of saturated critical heat flux in a single, uniformly heated microchannel, Exp. Therm. Fluid Sci. 30 (2006) 765–774, https://doi.org/10.1016/J.EXPTHERMFLUSCI.2006.03.006.
[39] J.E. Park, Critical Heat Flux in Multi-Microchannel Copper Elements with Low Pressure Refrigerants, , Thesis,, École Polytechnique Fédérale de Lausanne, 2008.
[40] Z. Anwar, B.E. Palm, R. Khodabandeh, Dryout characteristics of natural and synthetic refrigerants in single vertical mini-channels, Exp. Thermal Fluid Sci. 68 (2015) 257–267, https://doi.org/10.1016/J.EXPTHERMFLUSCI.2015.04.016.
[41] C.B. Tibiriçá, D.M. Rocha, I.L.S. Sueth, G. Bochio, G.K.K. Shimizu, M.C. Barbosa, S. dos S. Ferreira, A complete set of simple and optimized correlations for microchannel flow boiling and two-phase flow applications, Appl. Therm. Eng. 126 (2017) 774–795, https://doi.org/10.1016/j.applthermaleng.2017.07.161.
[42] C.B. Tibiriçá, S. Szczukiewicz, G. Ribatski, J.R. Thome, Critical heat flux of R134a and R245fa inside small-diameter tubes, Heat Transfer Eng. 34 (2013) 492–499, https://doi.org/10.1080/01457632.2012.722457;WEBSITE:WEBSITE:TFOPB;PAGEGROUP:STRING:PUBLICATION.
[43] A.H. Al-Zaidi, M.M. Mahmoud, T.G. Karayiannis, Flow boiling of HFE-7100 in microchannels: experimental study and comparison with correlations, Int. J. Heat Mass Transf. 140 (2019) 100–128, https://doi.org/10.1016/j.ijheatmasstransfer.2019.05.095.
[44] J.J. Widgington, A. Ivanov, T.G. Karayiannis, Flow boiling heat transfer in a single microchannel and comparison with correlations, Int. J. Heat Mass Transf. 251 (2025) 127388, https://doi.org/10.1016/J.IJHEATMASSTRANSFER.2025.127388.
[45] A.H. Al-Zaidi, T.G. Karayiannis, Flow boiling in micro-pin fin heat exchangers and comparison with correlations, Appl. Therm. Eng. 283 (2026) 129008, https://doi.org/10.1016/J.APPLTHERMALENG.2025.129008.
[46] W. Li, J. Ma, T. Alam, F. Yang, J. Khan, C. Li, Flow boiling of HFE-7100 in silicon microchannels integrated with multiple micro-nozzles and reentry micro-cavities, Int. J. Heat Mass Transf. 123 (2018) 354–366, https://doi.org/10.1016/J.IJHEATMASSTRANSFER.2018.02.108.
[47] A.H. Al-Zaidi, M.M. Mahmoud, T.G. Karayiannis, Flow boiling in copper and aluminium microchannels, Int. J. Heat Mass Transf. 194 (2022), https://doi.org/10.1016/J.IJHEATMASSTRANSFER.2022.123101.
[48] R.K. Shah, A.L. London, Laminar Flow Forced Convection in Ducts : A Source Book for Compact Heat Exchanger Analytical Data, 1st ed., Academic Press, New York, 1978.
[49] H.W. Coleman, W.G. Steele, Experimentation, Validation, and Uncertainty Analysis for Engineers: Third Edition, John Wiley and Sons, 2009, https://doi.org/10.1002/9780470485682.
[50] P.X. Jiang, M.H. Fan, G.S. Si, Z.P. Ren, Thermal–hydraulic performance of small scale micro-channel and porous-media heat-exchangers, Int. J. Heat Mass Transf. 44 (2001) 1039–1051, https://doi.org/10.1016/S0017-9310(00)00169-1.
[51] P.S. Lee, S.V. Garimella, Thermally developing flow and heat transfer in rectangular microchannels of different aspect ratios, CTRC Research Publications 49 (2006) 3060–3067, https://doi.org/10.1016/j.ijheatmasstransfer.2006.02.011.
[52] D. Copeland, Optimization of parallel plate heatsinks for forced convection, Annual IEEE Semiconductor Thermal Measurement and Management Symposium, IEEE, 2000, pp. 266–272, https://doi.org/10.1109/stherm.2000.837093.
[53] A.H. Al-Zaidi, M.M. Mahmoud, A. Ivanov, T.G. Karayiannis, Bubble nucleation site density, generation frequency and departure diameter in flow boiling of HFE-7100, Int. J. Heat Mass Transf. 242 (2025) 126830, https://doi.org/10.1016/J.IJHEATMASSTRANSFER.2025.126830.
[54] C.K. Guan, J.F. Klausner, R. Mei, A new mechanistic model for pool boiling CHF on horizontal surfaces, Int. J. Heat Mass Transf. 54 (2011) 3960–3969, https://doi.org/10.1016/J.IJHEATMASSTRANSFER.2011.04.029.
[55] S. Dahariya, A.R. Betz, High pressure pool boiling: mechanisms for heat transfer enhancement and comparison to existing models, Int. J. Heat Mass Transf. 141 (2019) 696–706, https://doi.org/10.1016/J.IJHEATMASSTRANSFER.2019.07.016.
[56] A. Donniacuo, R. Charnay, R. Mastrullo, A.W. Mauro, R. Revellin, Film thickness measurements for annular flow in minichannels: description of the optical technique and experimental results, Exp. Therm. Fluid Sci. 69 (2015) 73–85, https://doi.org/10.1016/J.EXPTHERMFLUSCI.2015.07.005.
[57] R. Charnay, J. Bonjour, R. Revellin, Experimental investigation of R-245fa flow boiling in minichannels at high saturation temperatures: flow patterns and flow pattern maps, Int. J. Heat Fluid Flow 46 (2014) 1–16, https://doi.org/10.1016/J.IJHEATFLUIDFLOW.2013.12.002.
[58] S. Saisorn, J. Kaew-On, S. Wongwises, Flow pattern and heat transfer characteristics of R-134a refrigerant during flow boiling in a horizontal circular mini-channel, Int. J. Heat Mass Transf. 53 (2010) 4023–4038, https://doi.org/10.1016/J.IJHEATMASSTRANSFER.2010.05.022.
[59] H. Liu, Z. Ma, L. Zhang, K. Li, Q. Lian, L. ming Pan, Minimum entropy production principle-based semi-empirical model for void fraction prediction in vertical upward dispersed gas-liquid flows, Int. J. Heat Mass Transf. 247 (2025) 127120, https://doi.org/10.1016/J.IJHEATMASSTRANSFER.2025.127120.
[60] S.M. Zivi, Estimation of steady-state steam void-fraction by means of the principle of minimum entropy production, J. Heat Transfer 86 (1964) 247–251, https://doi.org/10.1115/1.3687113.
[61] R.S. Patel, J.A. Weibel, S.V. Garimella, Mechanistic modeling of the liquid film shape and heat transfer coefficient in annular-regime microchannel flow boiling, Int. J. Heat Mass Transf. 114 (2017) 841–851, https://doi.org/10.1016/j.ijheatmasstransfer.2017.06.121.
[62] E.O. Moeck, Annular-Dispersed Two-Phase Flow and Critical Heat Flux, , PhD Thesis,, McGill University, 1970.